Characterizing atmospheric stability in complex terrain

Nathan J. Agarwal[1] and Julie K. Lundquist[1,2]

[1]Department of Earth and Planetary Sciences, Johns Hopkins University, Baltimore, MD, USA
[2]National Laboratory of the Rockies, Golden, CO, USA

Correspondence: Nathan J. Agarwal (nagarw22@jh.edu)

Abstract. Characterizing atmospheric stability becomes challenging in heterogeneous complex terrain. We use data from 47 meteorological towers associated with the Perdigão field campaign to recommend data processing approaches and to assess the limitations of shorter or fewer towers. We quantify atmospheric stability according to the Obukhov ~~length~~Length, the turbulence kinetic energy, and the turbulence dissipation rate using ~~a range of decomposition periods~~two decomposition periods, including consistent 10 minute periods to match convention in the wind energy community and consistent 30 minute periods to match convention in the atmospheric science community. ~~Atmospheric stabilitycharacterization is impacted by the Reynolds decomposition period, so care should be taken to use appropriate intervals~~We also demonstrate a methodology that can indicate the necessary number and location of towers to characterize atmospheric stability. We find that the 10 minute Reynolds decomposition window underestimates turbulence patterns. Additionally, 10 m measurements do not provide reliable 100 m hub-height stability predictions. ~~Finally, we demonstrate a methodology that can indicate the necessary number and location of towers to characterize atmospheric stability.~~ Holistically, this work addresses challenges in relying on sparse surface measurements.

 Funding was provided by the U.S. Department of Energy Office of Critical Minerals and Energy Innovation Wind Energy Technologies Office.

1 Introduction

The atmospheric boundary layer (ABL) directly interacts with Earth's surface, and the surface/atmosphere interactions that occur in this layer dictate transport of heat, momentum, sediment, and moisture into the larger atmosphere (Stull, 1988). Understanding these exchange processes has implications for fields like renewable energy (Pérez Albornoz et al., 2022) and agriculture (Tang et al., 2022). These exchange processes are also highly dynamic and sensitive to atmospheric stability (Garratt, 1994).

Atmospheric stability ~~describes~~ controls how the atmosphere responds to disturbances, affected by buoyancy and/or mechanical forcing. Static stability considers how buoyancy or temperature gradients may affect a vertically perturbed air parcel. A region of the atmosphere is statically stable if a perturbed parcel in that region ~~is restored back~~ experiences restoring forces toward its equilibrium height, statically unstable if the air parcel rises away from its equilibrium height, and neutral if the air parcel is unaffected. Dynamic stability considers the effects of both buoyancy and wind shear processes to determine whether a flow will become turbulent. Statically stable flows can be dynamically unstable and can become turbulent if the wind shear is strong enough. Thus, laminar flow exists only if the layer of air is stable both dynamically and statically (Stull, 1988; Angevine et al., 2020). ~~Because both static and dynamic stability address key characteristics of the wind resource, atmospheric stability~~ Atmospheric stability characterization remains an active field of study ~~.~~ for fields like wind energy (Pérez Albornoz et al., 2022) .

~~Atmospheric stability affects wind power generation. Optis and Perr-Sauer (2019) implemented several machine-learning methods to assess the relative importance of meteorological variables in wind farm energy assessments and found atmospheric stability to be one of the most important variables of those considered, regardless of the model used. Stability-driven differences in power generation have been documented for both onshore and offshore projects and may affect turbines differently, depending on the turbine's relative location. Wharton and Lundquist (2012) analyzed turbine power generation data for a west coast North American wind farm in channeled flow and found average power generation differences between stable and unstable cases approaching 15%. Pérez et al. (2023) analyzed meteorological mast and marine buoy data for a Yucatan coastal site and found 17% difference in power output between stable and unstable conditions. Radünz et al. (2021) investigated two wind farms in the complex Morrinhos site in Northeast Brazil and found that while the front rows outperformed the back rows during daytime unstable conditions, the back rows outperformed the front rows during the nighttime very stable conditions.~~

Atmospheric stability ~~also~~ affects wind power generation through the effects of turbulence~~intensity~~, shear, and veer~~(Lundquist, 2022)~~ . In very early work, Elliott (1990) ~~analyzed power curves for three turbines and~~ showed that significant errors in power curve measurements can result if the stability-influenced effects of wind shear and turbulence are ignored. ~~Later, Vanderwende and Lundquist (201~~ ~~analyzed nacelle and meteorological tower measurements from a wind farm in the high plains of central North America and~~ Wharton and Lundquist (2012) showed that stable conditions led to turbine overperformance. At a different, high plains location, Vanderwende and Lundquist (2012) found that stable conditions were associated with reduced power performance~~of up to 6%.~~.Similarly, Bardal et al. (2015) ~~analyzed lidar and meteorological mast data for a central Norwegian coastal wind farm and~~ found reduced power in the middle of the power curve for cases with shear exponents greater than 0.15 ~~. Gao et al. (2021) collected five years of data at the Eolos facility in Minnesota and also~~ for a coastal site. At a flat terrain site, Gao et al. (2021) found that the shape of the wind veer profile affects differences in power performance. Sanchez Gomez and Lundquist (2020) studied power production at an onshore wind power plant ~~with a strong diurnal cycle~~ in flat terrain and found that while large values of wind veer were associated with turbine underperformance, large shear values with small values of wind veer were associated with turbine overperformance, resolving the apparent contradiction between Wharton and Lundquist (2012) and Vanderwende and Lundquist (2012).

The stability-driven effects of turbulence, wind shear, and wind veer also affect turbine loads. ~~The aeroelastic simulations performed in Sathe et al. (2013)~~Sathe et al. (2013)showed that rotor and tower loads increase in high shear environments at both flat and ocean sites. Further, in Dimitrov et al. (2018), while wind shear was shown to strongly influence blade root loads ~~in surrogate load models calibrated with a database of high-fidelity load simulations,~~ veer showed only a minimal effect on fatigue loads for flat, forested, and mountainous sites. Wind shear also dominated the sensitivity analysis performed in Robertson et al. (2019) with 18 different parameters influencing blade root out-of-plane pitching moment and blade shaft bending moments. Putri et al. (2019) found that the fatigue damage of a spar-buoy offshore wind turbine is higher in unstable cases than in near-neutral cases.

Atmospheric stability also affects turbine wakes. Baker and Walker (1984) observed a slower wake recovery for a wind turbine under stable conditions ~~, and Iungo and Porté-Agel (2014) showed a faster wake recovery under convective conditions~~for a mountainous, forested site. Magnusson and Smedman (1994) showed a larger velocity deficit in stable conditions for a turbine ~~near the Alsvik wind farm.~~ in coastal conditions. Iungo and Porté-Agel (2014) also showed a faster wake recovery under convective conditions for a valley site surrounded by mountains. The scanning lidar measurements of Aitken et al. (2014) taken at a flat site downwind of complex terrain also found slightly stronger wake deficits in stable conditions even for a turbulent site, while the scanning lidar measurements of Bodini et al. (2017) for a flat Iowa site showed that wakes ~~are much more distinct~~ persist further in stable conditions. Wind turbine wakes also respond to the stability-driven effects of wind veer. Large-eddy simulation studies (Vollmer et al., 2016; Churchfield and Sirnivas, 2018), scanning lidar measurements (Bodini et al., 2017), and nacelle lidar measurements (Brugger et al., 2019) have shown that in the veering flow typical of stably stratified conditions, the wake will stretch into an 3D ellipse. Englberger and Dörnbrack (2018) ~~performed a detailed parameter large-eddy simulation study that~~ showed that increasing veer increases the erosion of the turbine wake in both flat and complex terrain. Stability-based effects on wake propagation also have secondary effects on turbine power generation (Barthelmie et al., 2013). Keck et al. (2014) compared the results of their dynamic wake meandering model to field observations and showed 22% differences in wake losses between stable and unstable conditions.

Given that atmospheric stability has implications for power generation, turbine loads, and wake propagation, determining optimal atmospheric stability definitions is critical for reliable wind resource assessments and wind energy forecasting (Optis and Perr-Sauer, 2019; Lee et al., 2020). However, multiple metrics exist to quantify stability. Some metrics, like the Obukhov ~~length~~Length (Monin and Obukhov, 1954), classify stability at a single altitude. Other metrics, like the bulk and gradient Richardson numbers, classify stability across a given vertical extent. Other metrics~~still, like the~~ , like turbulence kinetic energy (TKE) and turbulence dissipation rate (ϵ), characterize stability indirectly through turbulence (Stull, 1988). Some metrics also rely on determining an appropriate averaging window, and there are multiple~~ – sometimes conflicting –~~ , sometimes conflicting, approaches for defining the averaging window (Howell and Mahrt, 1994).

Financial constraints also inform challenges to atmospheric stability characterization. While meteorological towers can provide both the wind and temperature measurements required to assess atmospheric stability, the material costs for meteorological towers alone can cost on the order of $1 million for a 100 MW utility-scale onshore project (Eberle et al., 2019). Sonic anemometers to measure wind characteristics and thermometers to measure temperatures introduce additional costs. Thus, it

could be possible to reduce costs if surface stability assessments were more reliable in predicting hub-height stability without the need to invest in tall (i.e., 100 m) meteorological towers.

Complex terrain introduces further challenges to atmospheric stability classification ~~(Serafin et al., 2018; Cantero et al., 2022; Mosso et a~~ (Serafin et al., 2018; Cantero et al., 2022). Skillful wind forecasts in complex terrain are challenging, owing largely to the prevalence of heterogeneous terrain-modulated flows, such as mountain wakes, mountain waves, gap flows, valley cold pools, and mountain-valley circulations (Fernando et al., 2019). Despite these issues, many modeling efforts still rely on physical parameterizations developed over flat, horizontally homogeneous terrain because of constrained data availability (Stiperski and Rotach, 2016; Sfyri et al., 2018).

These complex terrain dynamics influence wind energy siting and further complicate wind energy assessments (Clifton et al., 2022). Lange et al. (2017) used a scale model in a three-dimensional wind testing chamber and showed that the mean wind, wind shear, and turbulence level are extremely sensitive to the exact details of the terrain, affecting the lifetime and maintenance costs of wind turbines. Han et al. (2018) ~~analyzed experimental data from a wind farm site in complex terrain in China and~~ found that complex terrain modifies the wind profiles, resulting in significant performance differences under both stable and unstable conditions. Despite their impact, these dynamics are still not captured well by commonly used commercial wind farm planning ~~computer~~ models (Shaw et al., 2019; Olson et al., 2019).

~~Financial constraints also inform challenges to atmospheric stability characterization. While meteorological towers can provide both the wind and temperature measurements required to assess atmospheric stability, the material costs for meteorological towersalone can cost on the order of $1 million for a 100 MW utility-scale onshore project (Eberle et al., 2019). Sonic anemometers to measure wind characteristics and thermometers to measure temperatures introduce additional costs. Thus, it could be possible to reduce costs if surface stability assessments were more reliable in predicting hub-height stability without the need to invest in tall (i.e., 100 m) meteorological towers~~ The Perdigão field campaign (Fernando et al., 2019) provided a comprehensive dataset for studying flow in complex terrain. Extensive instrumentation across the Vale do Cobrão enabled new insights into recirculation, gustiness, low-level jets, and mountain waves, as well as wind-energy-relevant phenomena such as wake deflection and wake self-similarity, as discussed in detail below. The Perdigão measurements have also supported major advances in modeling, including long-term WRF-LES simulations, improved terrain and canopy representations, turbulence-initiating CPM approaches, and virtual-lidar emulation. In parallel, Perdigão spurred development of multi-lidar scanning strategies and virtual-tower methods that extend measurement capabilities aloft.

Despite these advances, existing Perdigão analyses share two important limitations. First, most focus on vertical extrapolation, virtual towers, and rotor-layer prediction while largely neglecting how horizontal heterogeneity imposed by steep terrain and vegetation modulates near-surface flow. Second, although technological solutions have enabled reliance on measurements above 40–80 m, the representativeness of surface or 10 m observations remains poorly understood. This gap directly affects wind-energy stakeholders, who often depend on near-surface measurements for resource assessment and may be unable to deploy tall towers in complex terrain.

~~This work addresses the representativeness of stability metrics by assessing~~ These limitations motivate the present study. We evaluate the representativeness of Perdigão's 10 m surface measurements using three stability metrics ~~based on~~ and assess

their ability to capture ~~changes in time, height, and terrain. Based on the results from this analysis, this work offers guidance to meteorologists and other stakeholders that may be interested in analyzing complex terrain sites. This manuscript is organized as follows. The Perdigão field campaignis introduced, the data preparationis described, and both the metricsand evaluation criteria are outlined in Sect. 2. Then, the results from these assessments are presented in Sect.~~ temporal variability, vertical structure, and terrain-driven heterogeneity. The resulting guidance informs both meteorological analysis of complex terrain and practical tower-siting decisions for wind-energy applications. Section 2 describes the field campaign, data preparation, and metrics; Sections 3 and ~~discussed in Sect. 4. Finally, conclusions are drawn and recommendations are offered in Sect. 5.~~ 4 present and discuss results; Section 5 concludes with recommendations.

2 Data and methods

2.1 Perdigão field campaign

The Perdigão field campaign, which occurred 1 May–15 June 2017, was a scientific research effort near the town of Perdigão in central Portugal. This international collaboration addressed knowledge gaps surrounding the microscale details of winds in complex terrain by collecting a comprehensive, high-resolution dataset of meteorological quantities for the site (Fernando et al., 2019). The field campaign took place in the Vale do Cobrão, with an approximately two-dimensional valley and parallel ridges with annual 10 m wind climatology perpendicular to the ridges (Fig. 1).

Perdigão addressed fundamental understandings of physical mechanisms in complex terrain. Menke et al. (2019) documented recirculation zones throughout the valley with doppler radar data. Letson et al. (2019) used data from both sonic anemometers and Doppler lidars to assess wind gust characteristics. Wagner et al. (2019) as well as Wildmann et al. (2019) and Venkatraman et al. (2023) analyzed detection of low-level jets (LLJs). Wise et al. (2021) documented mountain wave patterns further studied by Robey and Lundquist . This field campaign has also supported research into wind-energy-specific processes like wind turbine wakes. Menke et al. (2018) used data from six scanning lidars to analyze the dependence of wake deflection patterns on the atmospheric stability, and these wake deflection patterns were also scrutinized by Barthelmie and Pryor (2019) and Wise et al. (2021). Similarly, Dar et al. (2019) simulated the wake behind a turbine and showed that the self-similarity of the wake implied that the wake pattern depended on neither the complexity nor the shape of the terrain.

Improving the understanding of these physical mechanisms has also enabled model improvement. Wagner et al. (2019) established a foundation with a long-term albeit coarse Weather Research and Forecasting (WRF) large eddy simulation (LES) simulation set for the full observational period. Palma et al. (2020) developed a digital terrain model (DTM) for the site and also defined a necessary horizontal grid cell spacing criteria of 40 m to appropriately characterize the site. Several modeling works have also expanded upon this need for improved representation of horizontal variability for the region. Quimbayo-Duarte et al. (2022) established a forest canopy parameterization for the WRF-LES model that improved wind modeling within the lowest 500 m of the atmosphere and attributed the imposed drag parameterization to a need for even higher-resolution land surface inputs. Venkatraman et al. (2023) altered the forest canopy parameterization to consider more realistic (i.e. shorter) heights in a set of OpenFOAM simulations. Finally, Al Oqaily et al. (2025)—building upon the ensemble

models in Giani and Crippa (2024)—again underscored the importance of land cover in an additional set of LES simulations. Connolly et al. (2021) demonstrated the utility of the cell perturbation method (CPM) (Muñoz-Esparza et al., 2015) in capturing flow features in LES simulations of the region, especially in weakly convective conditions. The Perdigão field campaign has also enabled improvements in wind turbine specific modeling in complex terrain. Wise et al. (2021) introduced the WRF-LES-GAD to the Perdigão dataset, and leveraging the output from this model, Robey and Lundquist (2024) demonstrated the utility of a virtual lidar model (Robey and Lundquist, 2022) in simulating range height indicator (RHI) scans. The modeling improvements have also extended beyond numerical weather prediction (NWP) models. Barthelmie and Pryor (2019) developed a novel detection algorithm that could both identify and characterize wake patterns, Vassallo et al. (2020) used artificial neural networks (ANNs) to improve wind speed error by up to 52%, Bodini et al. (2020) used machine-learning models to reduce the average error in model representation of turbulence dissipation rate by up to 40%, and Mosso et al. (2025) predicted turbulence anisotropy for the region using random forest models.

The Perdigão field campaign has also enabled improvements in measurement techniques. Vasiljević et al. (2017) outlined a methodology for multi-lidar Doppler lidar experiments and Wildmann et al. (2019) presented a new wake measurement strategy that used three synchronized lidars to adapt to the prevailing wind direction automatically. Bell et al. (2020) combined multiple Doppler lidar scans to create virtual towers that could extend beyond the range of traditional in situ meteorological towers. Coimbra et al. (2025) also performed a virtual mast analysis of the Perdigão region with three coordinated dual lidar. These measurements allowed for not only the mean quantity comparisons available in Bell et al. (2020), but also turbulent quantities as well.

2.2 Perdigão field campaign measurements

Multiple instruments were deployed throughout the field campaign. Instrumentation included 49 meteorological towers, radiosondes, lidars, two tethered lifting systems, and additional instrumentation including radars and radiometers (Fernando et al., 2019).

The meteorological towers provide the ~~data~~ main data source for this analysis. ~~Of~~ 47 of the 49 towers ~~, 47~~ included a 20 Hz sonic anemometer at the 10 m ("surface") level. ~~Of~~ 18 of these 47 towers ~~, 18~~ also included a 1 Hz thermometer at this 10 m level, although the only 10 m temperature measurements that were used for this analysis were from the three 100 m towers. All towers were constructed to minimize flow distortion by the tower. In cases where local obstacles interfered with the anemometer location, the anemometer boom was set to point down-valley. Booms on the towers pointed toward directions varying between 111 and 166 degrees. The azimuth, pitch, roll, and height of the sonic anemometer mounting booms were measured and recorded. The sonic anemometer data were then tilt-corrected using the ~~double-rotation~~ planar fit method following the approach of Wilczak et al. (2001).

The three 100 m towers were strategically placed to sample flow conditions within differing terrains. Specifically, tse04 was located on an exposed ridge on the southwest, tse09 in the valley with eucalyptus and fir trees, and tse13 on a ridge with a heterogeneous canopy to the northeast (Table 1). Although translating CORINE Land Cover data (Bossard et al., 2000) into U.S. Geological Survey land use types to obtain surface roughness lengths (Pineda et al., 2004) suggests surface roughness

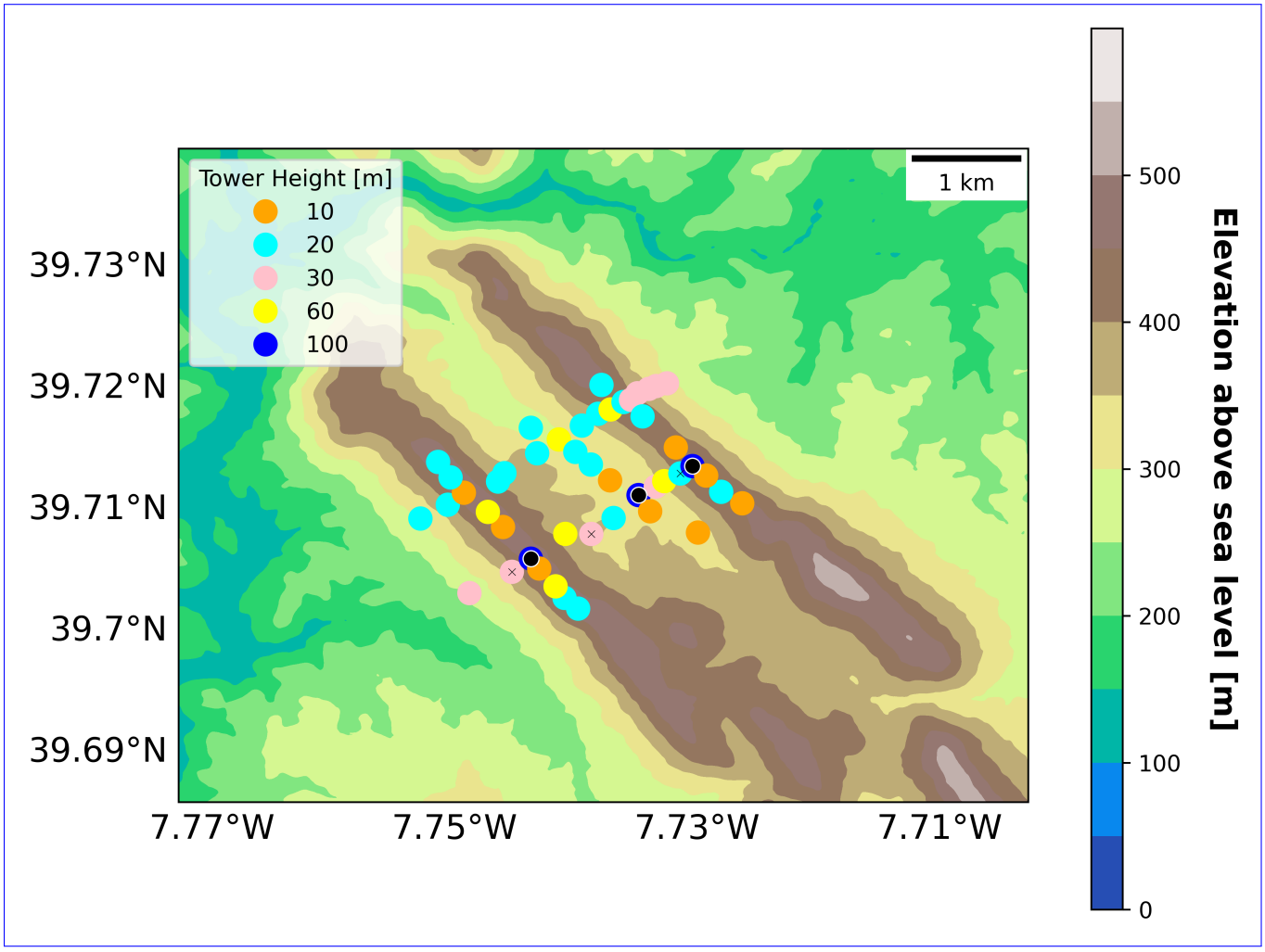

Figure 1. Topographic map of the Perdigão valley field campaign site with meteorological towers included. 100 m towers are additionally marked with a black circle and their corresponding radiometer measurements are indicated with an "X". Extensive other instrumentation are not depicted.

lengths on the order of 0.01–0.05 m, Wise et al. (2021), Wagner et al. (2019), and Palma et al. (2020) (among many others) have suggested that larger surface roughness lengths are more appropriate for the site. The mean canopy heights–as documented in Letson et al. (2019)–are below 10 m (Table 1 and Fig. 2), although individual trees may extend to 15 m (Mosso et al., 2025).

For each 100 m tower, 20 Hz sonic anemometers and 1 Hz temperature sensor measurements were collected at 10, 20, 40, 60, 80, and 100 m (Fernando et al., 2019; EOL, 2019), among other measurements. The 60 m temperature measurements for tse13 (NE ridge) were not used here due to their ~~high~~ frequent (76%) data unavailability.

Table 1. Shortname Reference for 100 m towers

height**Tower**	**Shortname**	**Topography**	**Location [WGS84]**	**Elevation above sea level [m]**	**Mean canopy height [m]**
tse04	Southwest Ridge	Turbine Ridge	7°44′33.37″W 39°42′21.47″N	473	1.5
tse09	Valley	Valley	7°44′5.40″W 39°42′40.36.″N	305	5.4
tse13	Northeast Ridge	Canopy Ridge	7°43′49.38″W 39°42′48.97.″N	453	3.6

2.3 Data preparation

The analysis presented herein relies on the 20 Hz sonic anemometer and 1 Hz air temperature sensor measurements from the meteorological towers ~~. These tilt-corrected data were also screened for quality assurance according to standard sensor error flags, with the most prevalent flag being the effect of rain~~ (EOL, 2019). These data were also screened for ~~additional quality controlspecific to this analysis~~quality control. Notably, data that suggested tower wake effects from the booms were removed ~~by identifying the boom orientation and removing any associated data~~ within 60 degrees (+/- 30 degrees) ~~of the boom orientation~~based on the process outlined in McCaffrey et al. (2017). These screening processes collectively removed 3.2% of the 20 Hz data. Block-averaged fluxes (Babić et al., 2016; Wildmann et al., 2019) were then calculated using an eddy-covariance approach (Aubinet et al., 2012) from the surviving data for all heights using two different Reynolds decomposition times, discussed below in "Reynolds Decomposition Time". The stability and turbulence metrics were calculated from these fluxes.

Two stages of screening were also performed to account for shading effects. First, data on days with clouds or precipitation were screened out of the analysis. The Perdigão field log (Supplement to Fernando et al., 2019) continues a daily breakdown of the synoptic conditions according to eight European standard patterns defined in Santos et al. (2016). This field log, along with determining the relevant synoptic regime for a day, also notes relevant weather patterns, such as cloud presence and precipitation. Based on this analysis, we screen out any days that include low or medium clouds as well as those with fog or precipitation. In situations where these weather patterns only affect targeted hours of the day, we remove the entire day to avoid biasing diurnal patterns. The net result of this screening is that 22 of the 45 days are removed (Appendix A).

Radiometer measurements informed the second, terrain-based, shading screening. These measurements–located near the 100 m towers at tse02, tse07, and tse12–were collected at either 20 m or 30 m and reported at 5 min intervals. These (cloudless, as defined above) incoming shortwave radiation measurements were diurnally-averaged and compared to the amount of

Figure 2. Canopy cover for (a) tse04, (b) tse09, and (c) tse13. The image of tse04 was identified as a still photo in the Danish Technical University (DTU) Perdigão video (DTU Wind and Energy Systems, 2017) and the images of tse09 and tse13 can be found in the Perdigão data archive (EOL).

incoming shortwave radiation expected by the Ineichen-Perez clear sky model (Ineichen and Perez, 2002), as defined in the python package pvlib (Anderson et al., 2023). The residual (measured-expected) was then assumed to trace hours where terrain shading might be assumed to occur. Instead of discarding data associated with shading, by identifying inequitable patterns in solar exposure between the towers, we were able to tailor our definitions of "stable" and "unstable" to only focus on hours that were not affected by these differences. Shown later, these stable and unstable hour definitions also inform our determination of an appropriate Reynolds decomposition window for two of three stability metrics. Taken together, these two strict shading evaluations minimize spatial and temporal biases between towers and support a more equitable evaluation.

2.3.1 Metric selection

This analysis evaluates three stability metrics~~ the Obukhov length~~ : the Obukhov Length (L), turbulence kinetic energy (TKE), and the turbulence dissipation rate (ϵ). While many other stability metrics exist (Stull, 1988), this metric subset was selected to include a mix of both categorical and qualitative metrics and only metrics with a strong and consistent diurnal cycle.

The mix of categorical and qualitative metrics provides a means to ~~to~~ categorize stability behavior based on regime. For example, because the Obukhov ~~length~~ Length categorically represents atmospheric stability (i.e., stable vs. unstable), we can compare the values of another stability metric (TKE, for example) during periods where the Obukhov ~~length~~ Length is stable with those during periods where the Obukhov ~~length~~ Length is unstable.

The diurnal cycle restriction was designed to assess how well the metric captures diurnal variability in boundary layer behavior. For L, each period was classified with a stability based on Table 2. Then, for each hour of the day, the total number of cases for each stability bin was summed and then normalized by the total number of cases for that hour throughout the experiment. The TKE and ϵ diurnal cycles were analyzed as diurnal distributions. For all metrics, the diurnal test was applied to the data from the surface (10 m) and aloft (100 m) separately and evaluated qualitatively. Turbulence intensity, which is another common metric in the wind energy community, was shown to have a variable and inconsistent diurnal cycle and was excluded through this screening.

Richardson Numbers were also intentionally not employed for this analysis. While other analyses such as Menke et al. (2019) have relied on a gradient Richardson number to assess stability, here we avoid any layer-based stability characterizations. These metrics were excluded becausethese metrics are sensitive to how the layer is defined.

2.3.2 Obukhov length (L)

The Obukhov ~~length~~Length, L, is ~~proportional to~~ the height above the surface at which buoyant factors first dominate over mechanical shear production of turbulence:

$$L = \frac{-\overline{\theta_v} u_*^3}{\kappa g \overline{w'\theta_v'}} \tag{1}$$

where κ = 0.4 is the von Kármán constant; g = 9.81 m s^{-2} is the acceleration due to gravity; $\overline{w'\theta'_v}$ represents the heat flux (K m s^{-1}); $\overline{\theta_v}$ represents the average virtual temperature (K); and u_* denotes the friction velocity (m s^{-1}):

$$u_* = (\overline{u'w'}^2 + \overline{v'w'}^2)^{1/4} \tag{2}$$

(Monin and Obukhov, 1954). Both the heat flux and the friction velocity were calculated based on the eddy-covariance approach using the appropriate averaging window, and the heat flux was calculated using the sonic temperature perturbations, as in Burns et al. (2012). θ_v is defined as:

$$\theta_v = T_v(\frac{p_0}{p})^{R/C_p} \tag{3}$$

where T_v is the virtual temperature (K) approximated as the air temperature; p_0 is a reference pressure (Pa); p is the pressure at a given height (Pa); and $R/C_p \approx 0.286$. Herein, θ_v was approximated as the air temperature due to a lack of localized pressure and moisture measurements. Further, because not all 47 towers had temperature measurements available at 10 m, the virtual potential temperature for the horizontal homogeneity analysis (described later) was assumed to be a uniform 300 K. The L values were binned according to a schema adapted from Gryning et al. (2007) (Table 2).

Table 2. ~~Stability parameter~~ Obukhov Length binning classifications adapted from Gryning et al. (2007)

Category	Range
Very Stable	$0 \leq L < 200$
Stable	$200 \leq L < 500$
Near Neutral	$\|L\| \geq 500$
Unstable	-500 $< L \leq$ -200
Very Unstable	-200 < $L \leq$ -0

2.3.3 Turbulence kinetic energy (TKE)

TKE quantifies turbulence in the flow via covariances. The mean TKE, $\overline{TKE}$ (m^2 s^{-2}), is ~~described by~~calculated as:

$$\overline{TKE} = \frac{1}{2}[\overline{u'^2} + \overline{v'^2} + \overline{w'^2}] \tag{4}$$

where u', v', and w' (m s^{-1}) are the Reynolds perturbation components from the mean wind (Stull, 1988). In all cases, perturbations are based on a block averaging window over the relevant time period.

2.3.4 Turbulence dissipation rate (ϵ)

The turbulence dissipation rate, ϵ (m^2 s^{-3}), represents the rate at which TKE is dissipated or converted into heat (Stull, 1988) and was calculated using the structure function method (Piper and Lundquist, 2004; Muñoz-Esparza et al., 2018; Wildmann

et al., 2019). According to this method, ϵ is related to a second-order structure function, $D_U(\tau)$ by the following relation:

$$\epsilon = \frac{1}{U\tau}[aD_U(\tau)]^{\frac{3}{2}} \tag{5}$$

where U is the horizontal velocity (m s^{-1}), a = 0.52 is the Kolmogorov constant, τ is the temporal separation (s), and $D_U(\tau)$ is the structure function:

$$D_U(\tau) =< [U(t+\tau) - U(t)]^2 > \tag{6}$$

where <> denotes the ensemble average and τ was treated as 2 s, consistent with prior analyses (Bodini et al., 2018; Wildmann et al., 2019; Bodini et al., 2019). To calculate ϵ, every 30 s, a centered 2 min window of data was targeted. The structure function was applied to this 2 min window, and the average value of the relevant structure function was retained for each ϵ calculation. These data were maintained at a 30 s resolution both because ϵ varies on a shorter timescale than L or TKE and is also not defined by a Reynolds decomposition window.

2.3.5 Reynolds decomposition time

Both L and TKE require Reynolds decomposition calculations (Stull, 1988; Reynolds, 1895). In a Reynolds decomposition, any variable ψ is split into a mean $\overline{\psi}$ and a turbulent component ψ'. The separation between these two components is determined by the Reynolds decomposition averaging window. Because determining a Reynolds decomposition window that appropriately differentiates mean behavior from turbulent motions is consequential to the resultant stability characterization, many methods to determine the Reynolds decomposition window exist.

Both L and TKE decomposition windows were calculated according to both ~~the ogive method (Babić et al., 2012) (which resulted in~~ a 30 min window ~~)~~ and a 10 min window based on wind energy industry conventions (IEC). While we also considered using a variable window based on a multi-flux-resolution decomposition (MRD) approach (Howell and Mahrt, 1997), a previous investigation of the Perdigão dataset with the MRD determined that the MRD was insufficient, so we instead adopted a consistent 30 min averaging approach for this dataset (Mosso et al., 2025).

An appropriate averaging window was ~~first~~ determined using an ~~ogive method as described in Desjardins et al. (1989), Oncley et al. (1996), and Babić et al. (2012)~~ogive-type method, the Cumulative Flux Averaging-Window Convergence Method (CFAW-CM). While the ogive method (Desjardins et al., 1989; Oncley et al., 1996; Babić et al., 2012) identifies an appropriate Reynolds-averaging window through spectral integration of the flux cospectrum in the frequency domain, the convergence method determines the window in the time domain by identifying the averaging period beyond which additional low-frequency variability no longer contributes to the flux covariance. This assessment was performed to determine whether a uniform averaging period could be utilized for heat fluxes ($\overline{w'\theta'_v}$) and friction velocities ($\overline{u_*}$) across various heights, times of day, and tower locations. ~~The ogive method requires calculation of fluxes using several averaging periods and then defines an appropriate averaging period based on the frequency in which there are no more (or negligible) contributions to a flux covariance.~~ By evaluating the cumulative eddy flux contribution according to increasing averaging periods, an asymptote separates the local turbulent fluctuations from the larger-scale (mesoscale) fluctuations. For this dataset, heat flux and friction velocity values were

calculated at each height for each tower location according to 1, 5, 10, 20, 30, and 60 min Reynolds decomposition windows. All values for a given Reynolds decomposition period were then averaged to a single value for that averaging period. To differentiate between times of day, the heat flux values were ~~subset to 00–04 UTC and 12–16~~ divided into 00–02 UTC and 12–14 UTC to represent nighttime (assumed stable) and daytime (assumed unstable) values, respectively. Based on this analysis, we used a consistent 30 min Reynolds decomposition window for both stable and unstable cases at all towers.

Secondly, we considered the wind energy industry standard, which uses a constant 10 min averaging window (Bailey et al., 1997; IEC). This standard assumes a clear separation or "spectral gap" (Van der Hoven, 1957) between the large-scale mesoscale motions and the small-scale turbulence, which does not always exist (Larsén et al., 2013; Kang and Won, 2016; Larsen et al., 2018). ~~The 10 min averaging is intended to target only turbulence (Larsén et al., 2013; Kang and Won, 2016; Larsen et al., 201~~

2.4 Post-processing

2.5 ~~Postprocessing~~

~~Extrema were also~~ Extrema were screened out of the stability metric calculations. This screening process involved isolating the distribution of values for each stability metric according to a given Reynolds decomposition window and replacing values outside of a given threshold as NaN (not a number). A common 99.5th percentile threshold was established to simultaneously remove anomalous data and protect representative data. Further, time periods flagged according to one stability metric were not necessarily flagged according to another, ensuring that the representativeness of each stability metric could be evaluated independently.

The process to apply this extrema threshold was tailored to each metric. Obukhov Length L extrema were flagged by extrema in u_*, $\overline{w't'_c}$, and $\overline{\theta_v}$ (Eq. 1). This decision to flag the constituent variables of the Obukhov ~~length~~ Length as opposed to the Obukhov ~~length~~ Length itself both ensured consistency across all stages of the calculations and also avoided targeted removal of near-neutral cases. Collectively, this Obukhov ~~length~~ Length screening process removed ~~1.06~~1.16% of L values.

Friction velocity u_* extrema were identified as u_* values greater than the 99.5% of the 30 min u_* distribution (~~1.20~~ 1.15 m s^{-1}). The same (i.e., ~~1.20~~ 1.15 m s^{-1}) 30 min u_* threshold was also applied to the 10 min u_* distribution to avoid mischaracterizing larger 10 min u_* values as extrema.

Heat flux $\overline{w't'_c}$ extrema were identified according to a process similar to that used to identify extrema in u_*, although the $\overline{w't'_c}$ extrema were flagged on both sides of the distribution. The 30 min distribution determined both the 30 min and 10 min threshold for $\overline{w't'_c}$, as was the case with u_*. However, in contrast, $\overline{w't'_c}$ extrema were identified by flagging the most extreme 0.5th percentile of the positive and negative $\overline{w't'_c}$ values separately. This distinction based on the heat flux sign ensured that both stable and unstable cases were screened and that these screenings were independent. This screening identified data greater than ~~0.521~~ 0.582 K m s^{-1} and less than ~~-0.226~~ -0.179 K m s^{-1}. These screening values correspond to ~~633.6~~ 642.5 W m^{-2} and ~~-274.4~~ -218.0 W m^{-2}, assuming that the product of the density of moist air, ρ_{air}, and the specific heat of air, C_p, is 1216 W m^{-2} (K m s^{-1})$^{-1}$ (Stull, 1988).

Mean virtual potential temperature $\overline{\theta_v}$ extrema were also flagged on both sides of the distribution, although the underlying data considered for the $\overline{\theta_v}$ process differed from those considered for the u_* and $\overline{w't'_c}$ processes. While the u_* and $\overline{w't'_c}$ screening processes considered data from all 47 towers, the $\overline{\theta_v}$ screening process only considered temperature measurements from the three 100 m towers to determine a reliable screening threshold. This distinction was made to account for the inconsistent temperature availability across the site. The net result of this $\overline{\theta_v}$ screening was that $\overline{\theta_v}$ less than ~~280.47~~ 279.97 K or greater than ~~306.5~~ 307.39 K were flagged.

The TKE extrema screening process was most analogous to that employed for u_*. TKE greater than the 99.5th percentile of the 30 min distribution (~~5.83~~ 4.85 m^2 s^{-2}) were flagged. Because the TKE screening depended only on TKE itself, ~~0.37~~0.15% of TKE values were flagged. Finally, the $\log_{10}\epsilon$ extrema screening process removed data from the top (~~-0.509~~-0.505) and bottom (~~-5.45~~-5.51) 0.5th percentiles, again constituting 1% of $\log_{10}\epsilon$ values.

2.5 Stability assessment

The variability in atmospheric stability was evaluated with two criteria: hub-height predictive index (HHPI) and horizontal homogeneity (HoH). These criteria, described more fully below, collectively describe the sensitivity of stability in time, altitude, and spatial location.

Atmospheric stability was first evaluated based on the HHPI. The HHPI assessment was designed to assess how well surface-level classifications predicted classifications at a representative wind turbine hub height of 100 m. This assessment could provide insight into whether surface measurements could predict hub height behavior without the investment of a full 100 m tower. ~~The~~ While many representative heights may be potentially considered in a wind farm resource assessment, the hub height is one such representative measurement. Further, the hub height, with typical values near 100 m, aligns with the highest available measurement from the meteorological towers during the Perdigão field campaign. The vertical information propagation over the 100-m tower is also assumed to be much shorter than the Reynolds decomposition window. The L HHPI was calculated as the fraction of cases in which the surface value and the aloft value showed the same stability classification. The TKE and ϵ HHPI were represented by the linear regression R^2 between the surface and aloft values for each metric. The HHPI assessment was also extended to other intermediate heights present on the towers (i.e., 20, 40, 60, and 80 ~~, and 100~~ m). For this extension of the HHPI analysis, the regression or agreement classification was performed by treating each of the intermediate heights as the base height compared to the 100 m hub-height calculations. This HHPI assessment is also performed for a flat terrain field campaign as a point of comparison in Appendix B.

Each metric was also evaluated for HoH. This assessment was designed to quantify the smallest number and location of meteorological towers necessary to capture the site's variability in surface (10 m) stability. For each metric, all 47 towers with sonic anemometers were considered. Because only 18 of these towers had available 10 m temperature measurements, the virtual potential temperature was assumed to be a uniform 300 K for the Obukhov ~~length~~ Length calculation just for the HoH analysis. Thus, this analysis could not account for differences in virtual potential temperature that might occur between towers. ~~These~~ This approach to addressing the lack of available temperature measurements was determined optimal because other potential solutions–such as performing the analysis at either a shorter or taller height–further limited the number of

available towers or relied on data fully within the vegetation layer. Shifting to 20 m would only allow 38 of the 47 towers to be analyzed. Shifting to 30 m would only leave 17 towers. Analyzing 100 m would only leave 3 data points. These other solutions also devalued the assessment as a practical demonstration of how stakeholders could leverage surface-level measurements to inform site characterization. These 47 towers were then represented as a graph network, with a node for each tower location and the edge weights ~~as the surface stability correlations.~~ representing the strength of similarity in surface stability between any two given towers. This similarity metric S mapped the correlation in surface stability C_{ij} with only positive edge weights such that $S = \frac{(C_{ij}+1)}{2}$. The smallest number of meteorological towers were then determined based on the Louvain community detection algorithm (Blondel et al., 2008), as implemented by the NetworkX Python package (Hagberg et al., 2008). Note that the Louvain algorithm, unlike kNN methods, treats the number of clusters as an output instead of an input. The Louvain algorithm ~~determined which towers were~~ determines which towers are redundant by identifying tower subgroups and assigning each tower to one of these subgroups. ~~For this analysis, the number of subgroups corresponded to the number of necessary towers and towers within a given subgroup were considered redundant. Further, the~~ The Louvain community detection algorithm ~~was chosen because of its~~ also enforces (non)treatment of overlapping communities, further ensuring that each community is treated independently with a unique tower. While the Louvain community detection algorithm is also sensitive to several tuning parameters, we make no adjustments to the default modularity gain threshold (1e-7) or resolution (1) and introduce no artificial seeds or establish restrictions on the number of optimization cycles.

Another optimization was then employed on the available partitions to determine a potential optimal tower layout. This optimization, performed with the pulp python library (Mitchell et al., 2011), treats the available partitions as a standard Hitting set (Karp, 1972) problem. As such, all available partitions across metric and averaging period were analyzed to determine the minimum number of towers necessary to span the full partition set. This tower set, represented graphically with stars, is non-unique. Thus, while other layouts could be considered equally viable, the starred tower set represents one possible layout that requires the smallest number of towers.

The Louvain community detection algorithm was also applied separately to large-eddy simulation (LES) from Robey and Lundquist (202 . This analysis serves as a proof-of-concept implementation to demonstrate how this methodology can extend to model output. Both the methodology and results of this analysis are provided in Appendix C.

3 Results

3.1 Site characterization

3.1.1 ~~Ogive analysis~~

~~We recommend a uniform 30 min Reynolds decomposition window based on the results from the ogive analysis. Based on the ogives, a 30 min heat flux averaging period is supported for all heights and tower locations (Fig. 4a , d, and g). The heat flux ogive at all three tower locations show an asymptote between an averaging period of 20–30 min and a shift to mesoscale~~

~~fluctuations at an averaging period of 60 min. The heat flux ogives also reflect ridge/valley distinctions. The heat flux ogives for the two ridges (~~

3.1.1 Radiation analysis

Before proceeding with stability analysis, we ensured that influences like topographic shading of our measurements did not directly impact parts of our analysis. In particular, we ensured that our designated "stable" and "unstable" hours did not experience inequitable solar exposure between towers. Importantly, these designations also translated to our CFAW-CM convergence analysis, which informed the Reynolds decomposition window.

All three 100 m towers likely experience shading during some part of the day. The incoming shortwave solar radiation near all towers shows a typical diurnal cycle for a mid-latitude land-based site (Fig. 3). This diurnal cycle is defined by low (i.e. zero) incoming shortwave radiation in the late (18-24 UTC) and early morning (00-04 UTC) hours with an increase throughout the morning (05-11 UTC), a midday peak (12-14 UTC), and a late afternoon drop (15-17 UTC) (Fig. 3). Within this diurnal cycle, differences in solar exposure throughout the day emerge. These differences in solar exposure contribute to differences in residuals. While negligible positive residuals may reflect measurement uncertainties, negative residuals are assumed to reflect shading.

Both the morning (05-07 UTC) and early evening (15-17 UTC) experience shading (Fig. ~~4aand g) show both higher values and greater spread than the heat flux ogive for the valley~~3). Cloudy days (Fig. 3a,c,e) naturally exhibit more shading than cloudless days (Fig. 3b,d,f) near each of the three 100 m towers. This diurnal difference in shading is especially pronounced in the valley, where negligible shading is suggested during cloudless days (Fig. 43d).

~~Heat flux ogives at each 100 m tower (tse04 (SW ridge): a, b, c; tse09 (valley): d, e, f; tse13 (NE ridge): g, h, i) and each available height, for all (a, d, g), stable (0–4 UTC, b, e, h) and unstable (12–16 UTC, c, f, i) cases. Points represent the mean value for a tower/height combination and error bars represent the standard error. (a) tse04 overall (SW ridge), (b) tse04 (SW ridge) stable, (c) tse04 (SW ridge) unstable, (d) tse09 (valley) overall, (e) tse09 (valley) stable, (f) tse09 (valley) unstable, (g) tse13 (NE ridge) overall, (h) tse13 (NE ridge) stable, (i) tse13 (NE ridge) unstable.~~

~~A 30 min heat flux averaging period is also appropriate for stable (00–04 UTC) cases at all three~~ Non-cloud-based shading due to diurnal differences in solar exposure also influences the two 100 m ~~towers~~ ridge towers. While shading in the valley is only imposed by clouds (Fig. ~~4b,e, and h). The stable heat flux ogives~~ 3c,d), the two ridges show stronger terrain-induced shading (Fig. 43a,b,e,~~and h)show an asymptote at small averaging periods at all tower locations. The stable ogive on the NE ridge~~ f). Further, while the SW ridge experiences minimal terrain-induced shading in the early evening (Fig. ~~4h)shifts to mesoscale fluctuations at 60 min, and the stable ogive on the SW ridge~~ 3b), the NE ridge shows the strongest terrain-induced shading during both the early morning and early evening (Fig. ~~4b)shows a less-pronounced mesoscale shift at 60 min.~~ 3f). Local canopy effects may then contribute–but not-define–non-cloud shading. The NE ridge shows more diurnal shading than the SW ridge and also has a taller canopy cover. However, the valley has canopy cover but experiences no non-cloud shading. Further, the SW ridge, with a negligible canopy cover, does experience non-cloud shading. Thus, shading from the larger ridge topography may also be contributing to the experience diurnal shading. Regardless of the exact shading source, these

site-based differences in shading suggest that sites do not have equivalent diurnal exposure to the incoming solar radiation. Our CFAW-CM analysis, described below, accounts for these differences in solar exposure by restricting our analysis to cloudless days and our stable and unstable periods to 00-02 UTC and 12-14 UTC, respectively.

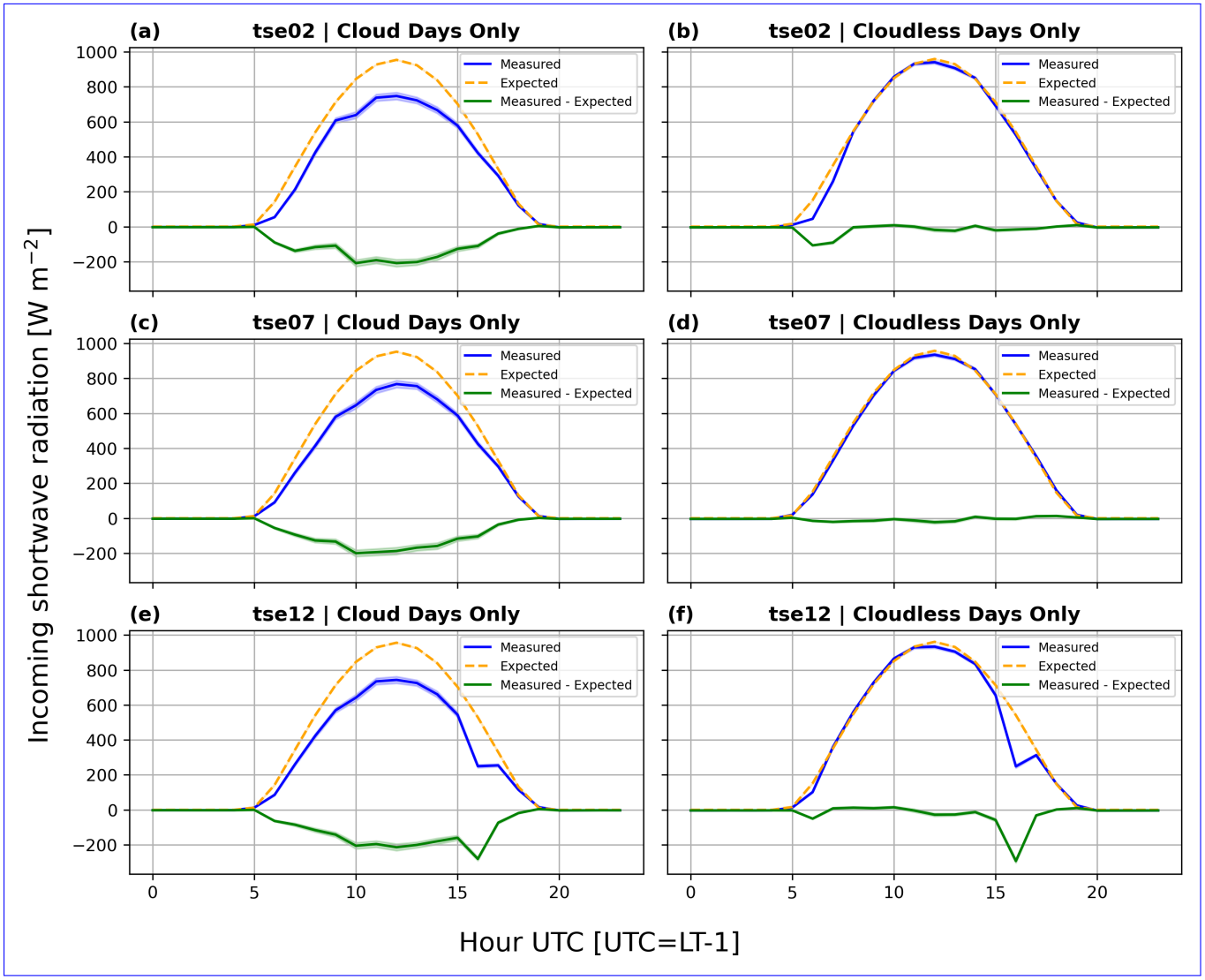

Figure 3. Comparison between expected and measured incoming shortwave radiation adjacent to each of the three 100 m towers. The line represents the mean value and the band represents the standard error. (a) tse02 (SW ridge) cloud days only; (b) tse07 (valley) cloud days only; (c) tse12 (NE ridge) cloud days only; (d) tse02 (SW ridge) cloudless days only; (e) tse07 (valley) cloudless days only; (f) tse12 cloudless days only.

3.1.2 Cumulative Flux Averaging-Window Convergence Method (CFAW-CM) analysis

We recommend a uniform 30 min Reynolds decomposition window based on the results from the CFAW-CM analysis. Most heights, sites, and metrics support this analysis, with a few exceptions.

The ~~stable ogives also reflect ridge /valley distinctions. The stable ogives on the two ridges (Fig. 4b and h) show larger values and a larger spread than the stable ogive for~~ CFAW-CM assessment as described above seeks to identify the Reynolds decomposition time long enough to incorporate all contributions by turbulence without including larger mesoscale contributions. This window is determined by identifying the asymptote before an increase assumed to be associated with mesoscale motions. For example, for heat flux in the valley (Fig. 4~~e), but the~~ d,e,f), values of the heat flux increase as the averaging time grows from 1 to 10 minutes, but constant between 10 and 30 ~~min period is still appropriate~~minutes, increasing at 60 minutes, thereby suggesting that an averaging period between 10 and 30 minutes is justifiable.

A 30 min ~~heat flux averaging period is also justified for unstable (12–16 UTC) cases~~ Reynolds decomposition period is consistently supported by valley observations. Friction velocities (Fig. 5d) increase sharply from 1-5 min, level from 5-30 min, and then sharply increase again at 60 min, indicating that 30 minutes captures turbulence fluctuations. This conclusion applies regardless of stability. Under stable conditions, valley heat fluxes (Fig. 4~~c, f, and i) . The unstable heat flux ogives at all three tower locations show asymptotic behavior that includes~~ e) remain small and nearly insensitive to averaging period longer than 5 min, while friction velocities (Fig. 5e) plateau between 20-30 min, before increasing at 60 min, again supporting a 30 min window. During unstable conditions, heat fluxes (Fig. 4f) level off after 10 min and increase again between 30-60 min whereas friction velocities (Fig. 5f) stabilize at 5 min before increasing again after 30 min. ~~The unstable ogives also reflect ridge/valleydistinctions. The unstable ogives~~ Together, these metrics confirm that a 30 min Reynolds decomposition period is appropriate in the valley, regardless of the stability condition.

A 30 min Reynolds decomposition period is also appropriate for most conditions on the two ridges. Under unstable stratification, both heat fluxes (Fig. 4c~~and i) show larger values and a larger spread than the unstable ogive for the valley~~ ,i) and friction velocities (Fig. 5c,i) consistently support a 30 min window. Heat fluxes (Fig. 4c,i) increase from 1-20 min before leveling off, while friction velocities show similar behavior. On the SW ridge, unstable friction velocities (Fig. 5c)–especially above 10 m–stabilize by 10 min, whereas on the NE ridge they increase until about 20 min at heights above 20 m and remain constant from 1-30 min at heights at or below 20 m) (Fig. ~~4f).~~

~~u_* ogives at each 100 m tower (tse04 (SW ridge): a, b, c; tse09 (valley): d, e, f; tse13 (NE ridge): g, h, i) and each available height, for all (a, d, g), stable (0–4 UTC, b, e, h) and unstable (12–16 UTC, c, f, i) cases, as in Fig. 4. Points represent the mean value for a tower/height combination and error bars are described with the standard error.~~

~~A~~ 5i). Together, these patterns justify a 30 min ~~friction velocity averaging period is generally justified across heights for the NE ridge and valley~~ decomposition period for unstable conditions on both ridges.

During stable conditions, the suitability of a 30 min window differs between the ridges. On the NE ridge, heat fluxes (Fig. ~~5d and g) . All friction velocity ogives for the valley~~ 4h) are mostly constant through 30 min before increasing from 30-60 min. Although friction velocities at 100 m continue to increase beyond 60 min, those at all other heights (Fig. 5~~d) and NE ridge~~ h)

behave more cleanly: they increase slightly from 1-20 min, plateau between 20-30 min, and then increase again between 30-60 min (Fig. 5g)and all but one ogive for h). Thus, a 30 min Reynolds decomposition period remains viable on the NE ridge, across metrics and stability conditions.

In contrast, stable conditions on the SW ridge are less well-represented by a 30 min window. Heat fluxes at 10-40 m continue to increase beyond 60 min, although those fluxes at 60-100 m are nearly constant from 1-30 min before jumping 30-60 min (Fig. 5a)show an asymptote at a 30 min averaging period. The friction velocity ogive at 10 m 4b). Stable friction velocities on the SW ridge increase steadily beyond 60 min at all heights, suggesting a need for a longer Reynolds decomposition window (Fig. 5a)does not asymptote at 30 min. The friction velocity ogives b).

The CFAW-CM analysis also highlights the contrasts between ridge and valley sites. Heat fluxes are larger and friction velocities are smaller on the ridges compared to those in the valley (Fig. 5a, d, and g)also differ by location. The friction velocity ogive in the valley 4 and Fig. 5). Valley heat fluxes (Fig. 4d) exhibit tighter spread than those on either ridge (Fig. 4a,g). Valley friction velocities (Fig. 5d) has the largest spread between heights of the three locations.

A 30 min friction velocity averaging period is also generally justified for stable (00–04 UTC) cases for increase with height whereas ridge friction velocities (Fig. 5a,g) decrease with altitude, with the exception of unstable friction velocities on the NE ridge (Fig. 5i) which resemble the valley (Fig. 5e)and for the NE ridge f). These site-based differences motivate further analysis in the following section.

3.1.3 Vertical profiles

Ridges and valleys reflect distinct profiles. Heat fluxes are larger on the two ridges than in the valley (Fig. 5h). The stable friction velocity ogives for these two locations show an asymptote for a 30 min averaging period and shift toward mesoscale fluctuations for a 60 min averaging period.One location that may suggest a need for a longer averaging period during stable cases is the SW ridge 6d). This distinction in heat flux magnitude is especially clear during unstable conditions (Fig. 6f), where the mean surface heat flux on the SW ridge is twice that in the valley. The unstable heat flux profile in the valley also reflects a sharp increase from 10 to 20 m that is not reflected for the two ridges (Fig. 6f). Instead, those along the two ridges decrease from the surface (Fig. 6f).

Stable heat flux profiles also reflect profoundly distinct shapes between the ridges and the valley (Fig. 6e). Stable heat flux profiles along the two ridges are more stable than in the valley at the surface, but as the height increases, the stable heat fluxes along the two ridges become increasingly weaker (Fig. 5b). The stable friction velocity ogives on the SW ridge 6e). In contrast, the stable heat flux profile in the valley (Fig. 5b) do not asymptote at 30 min, and the ogives continue to increase beyond a 60 min averaging period.

A 30 min friction velocity averaging period is also supported for all tower locations and heights during unstable (12–16 UTC)cases 6e) becomes more stable from the surface to 40 m before stabilizing above. Thus, while the valley is well-mixed during stable conditions, the ridges are not (Fig. 6e). This unique heat flux behavior in the valley during stable conditions is also corroborated by the heat flux CFAW-CM analysis, where stable heat fluxes in the valley (Fig. 5c, f, and i). The unstable friction velocity ogives at all tower locations show asymptotic behavior for a30 min averaging period and a shift

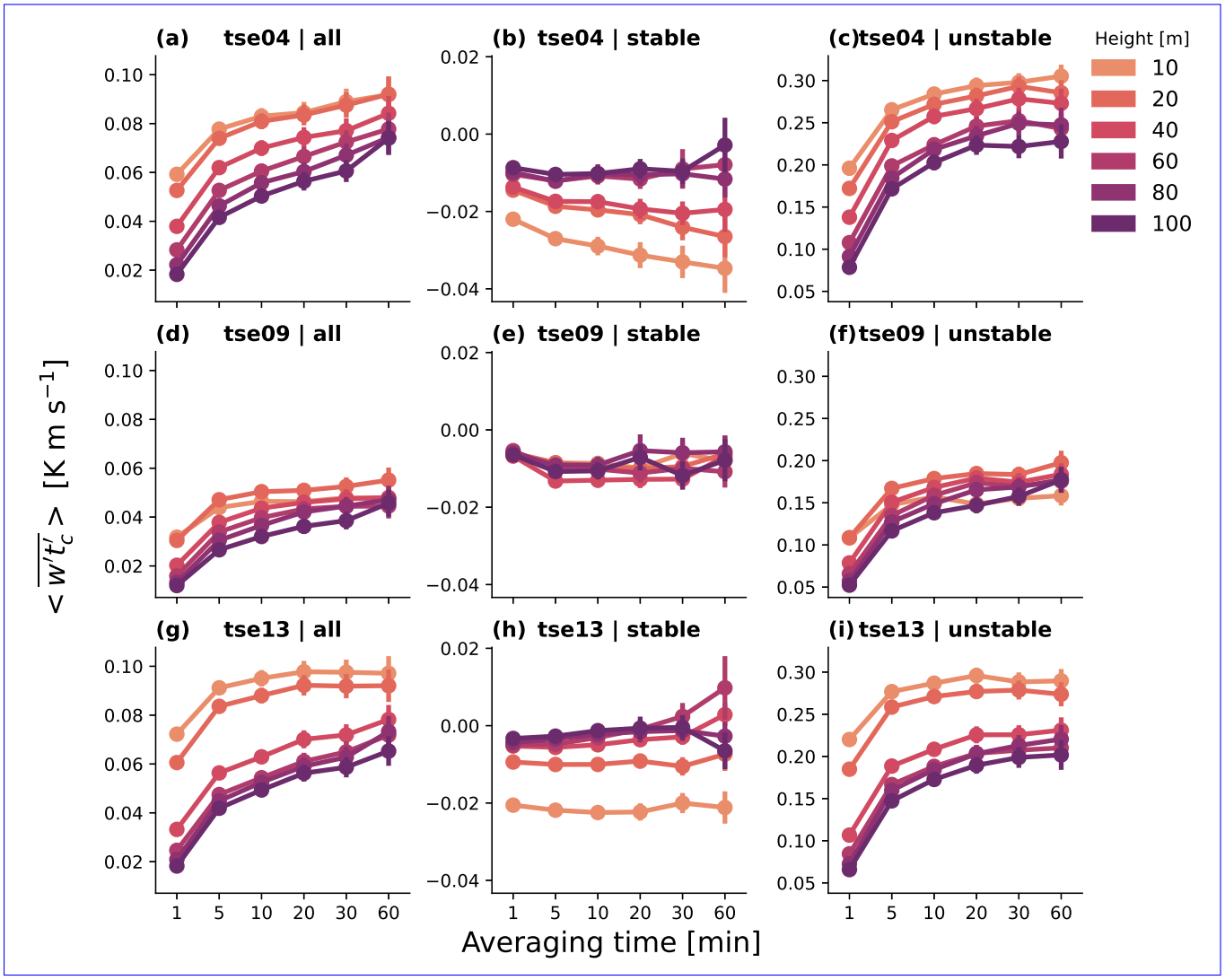

Figure 4. CFAW-CM analysis of heat fluxes at each 100 m tower (tse04 (SW ridge): a, b, c; tse09 (valley): d, e, f; tse13 (NE ridge): g, h, i) and each available height, for all (a, d, g), stable (0–2 UTC, b, e, h) and unstable (12–14 UTC, c, f, i) cases. Points represent the mean value for a tower/height combination and error bars represent the standard error. (a) tse04 overall (SW ridge); (b) tse04 (SW ridge) stable; (c) tse04 (SW ridge) unstable; (d) tse09 (valley) overall; (e) tse09 (valley) stable; (f) tse09 (valley) unstable; (g) tse13 (NE ridge) overall; (h) tse13 (NE ridge) stable; (i) tse13 (NE ridge) unstable.

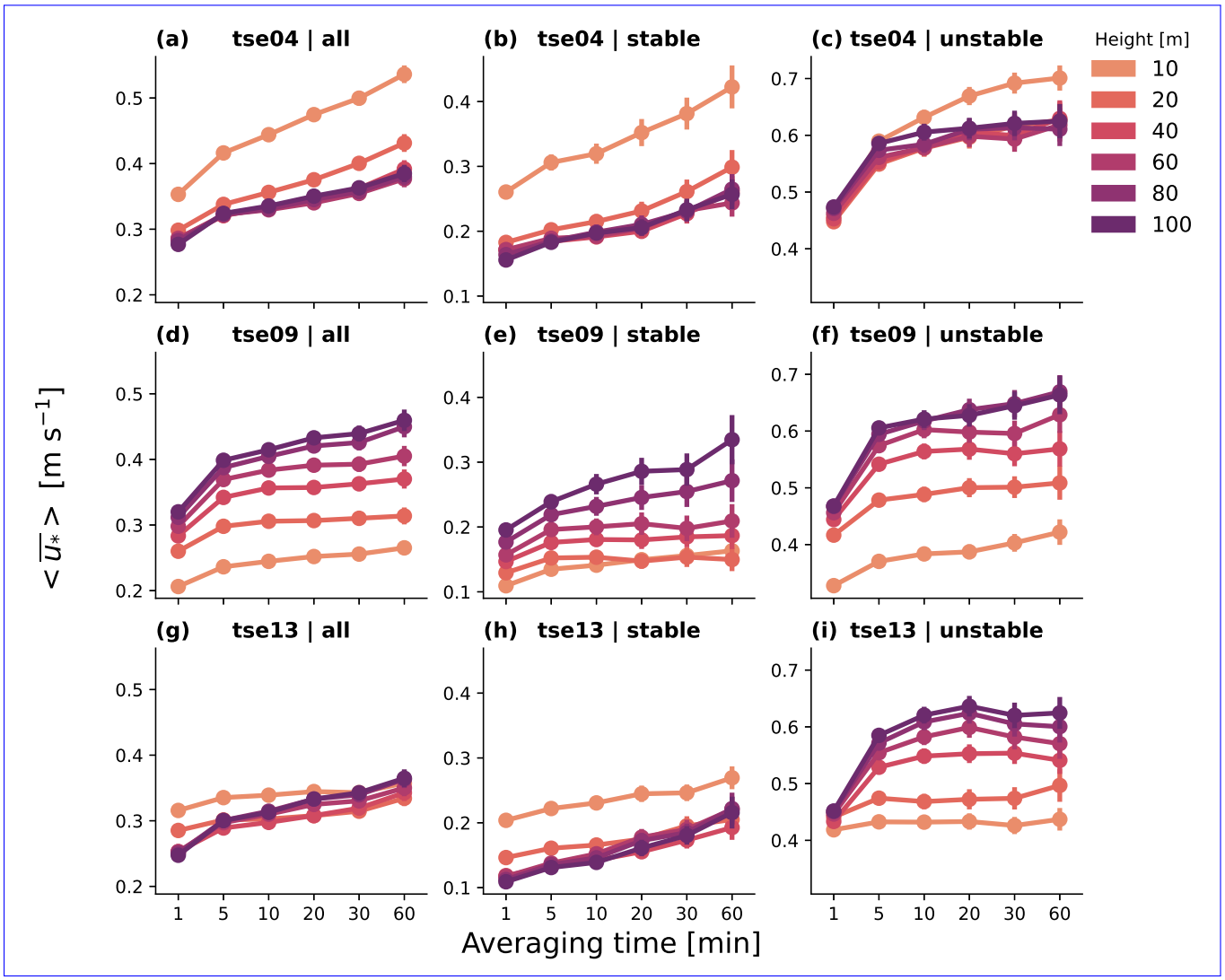

Figure 5. CFAW-CM analysis of u_* at each 100 m tower (tse04 (SW ridge): a, b, c; tse09 (valley): d, e, f; tse13 (NE ridge): g, h, i) and each available height, for all (a, d, g), stable (0–2 UTC, b, e, h) and unstable (12–14 UTC, c, f, i) cases, as in Fig. 4. Points represent the mean value for a tower/height combination and error bars are described with the standard error.

~~to mesoscale fluctuations for a 60 min averaging period.The unstable friction velocity ogives also reflect differences based on tower location.The unstable friction velocity ogive for~~ 4e) are much tighter and smaller than those along the two ridges (Fig. 4b,h). These ridge/valley differences in stable heat fluxes may signal an upside down boundary layer in the valley (Fig. 6e).

Ridge and valley distinctions are also reflected in the friction velocity profiles. Friction velocities begin larger at the surface along the two ridges and decrease before leveling 20-40 m (Fig. 6a). In contrast, valley friction velocities are smaller at the surface and increase aloft, eventually overtaking the friction velocities along the two ridges (Fig. 6a). These profile shapes are further reinforced for friction velocities during stable conditions (Fig. 6b).

Friction velocities during unstable conditions subvert these ridge and valley distinctions. Here, friction velocities on the NE ridge reflect those in the valley both in magnitude and in shape, increasing from a small surface value (Fig. 6c). In this case, only the SW ridge opposes the valley by demonstrating a ridge-like friction velocity profile (Fig. ~~5c)shows similar behavior across heights while the unstable friction velocity ogives for the valley (~~6c).

Both flow and terrain features may be contributing to this NE ridge subversion. Menke et al. (2019) documented recirculation zones during over half of the unstable periods. These flows could then explain why this unique behavior is reflected only during unstable cases. Menke et al. (2019) also documented that these recirculation flows occurred more frequently near the valley and NE ridge than the SW ridge. Thus, recirculation zones provide a mechanism that is aligned in terms of geography and stability condition to explain this behavior. Canopy effects may be also contributing to this NE ridge subversion. The NE ridge is, like the valley, covered with vegetation with a canopy (Table 1, Fig. ~~5f) and NE ridge(~~2c) that increases the surface roughness. In contrast, the SW ridge, which is more exposed (Table 1, Fig. ~~5i)show greater spread between heights.~~ 2a), may not have this potential. Quimbayo-Duarte et al. (2022); Venkatraman et al. (2023); Al Oqaily et al. (2025) have also all documented that increasing the surface roughness layer characterizations improves wind speed model performance for this region. Thus, the enhanced drag from the canopy may be reinforced by recirculation flows occurring during unstable conditions.

3.1.4 Wind roses and their spatial and vertical variability

Ridge and valley distinctions are also reinforced in winds. The 30 min wind roses for the three 100 m towers differ between the valley (Fig. 7c and d) and the ridges (Fig. 7a, b, e, and f). Both the SW (Fig. 7a) and NE (Fig. 7e) ridge surface winds show primarily a ~~southwesterly~~ northeasterly flow. In contrast, the surface valley winds (Fig. 7c) show primarily a southeasterly flow. Further, the surface valley winds (Fig. 7c) are slower than the surface winds on either of the two ridges (Fig. 7a and e)~~, likely due to sheltering effects.~~

. The wind roses for the three 100 m towers also differ between the 10 m surface winds and the 100 m winds. The 100 m winds at all three tower locations (Fig. 7b, d, and f) are ~~more diffuse~~ less bidirectional than the winds at their respective 10 m locations. The 100 m winds at all three tower locations are also generally faster and more consistent than the winds at their respective 10 m locations. These site and height distinctions between wind roses are also preserved, regardless of the averaging window (not shown).

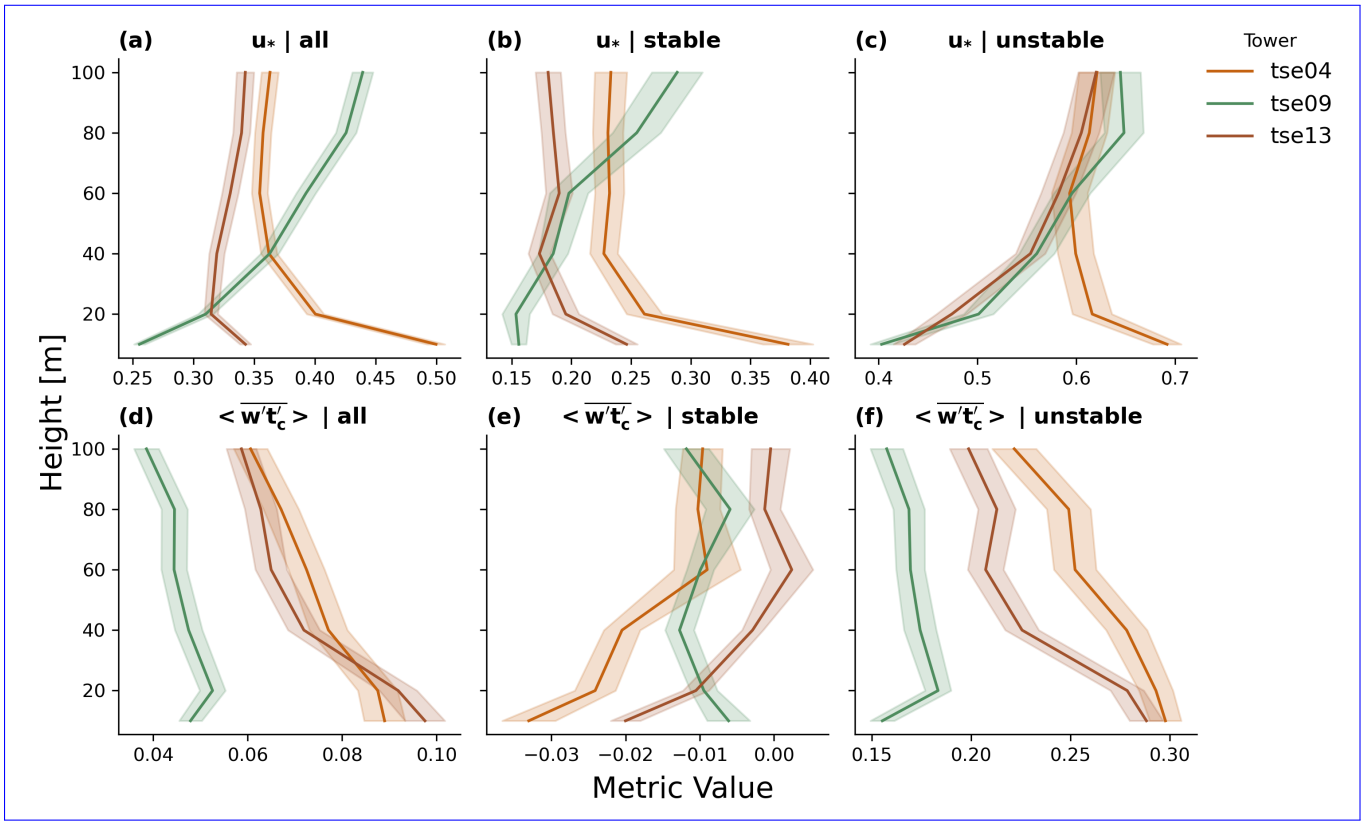

Figure 6. Perdigão field campaign vertical profiles with 30 min averaging at the three 100 m towers. The solid line indicates the mean value and the band represents the standard error. (a) friction velocity all (00-23 UTC); (b) friction velocity stable (00-02 UTC); (c) friction velocity unstable (12-14 UTC); (d) heat flux all (00-23 UTC); (e) heat flux stable (00-02 UTC); (f) heat flux unstable (12-14 UTC).

3.1.5 Diurnal variability

All three stability metrics exhibit a strong diurnal cycle (Figs. 8–15) as would be expected for this onshore mid-latitude region in late spring/early summer.

The L diurnal cycle (Fig. 8) differs between the ridges (Fig. 8a, b, e, f) and the valley (Fig. 8c, d). The L diurnal cycle shows mostly Stable (S) and Very Stable (VS) cases in the early morning (00–05 UTC) and evening (21–00 UTC) hours, with a shift toward mostly Unstable (U) and Very Unstable (VU) cases in the middle of the day (06–20 UTC) at all locations (Fig. 8). The valley L diurnal cycle is unique in its larger relative percentage of near-neutral cases aloft (Fig. 8d). ~~While the L diurnal cycle on the NE ridge (Fig. 8f) does contribute near-neutral cases aloft, this contribution is less extreme than that seen in the valley.~~ Further, the L diurnal ~~cycle on the SW ridge has~~ cycles on the two ridges have negligible near-neutral cases aloft (Fig. 8b). The L diurnal cycle in the valley is also unique in its reduction of the relative contribution of VU cases from the surface (Fig. 8c) to aloft (Fig. 8d). Again, while the L diurnal cycle on the NE ridge has more VU cases at the surface (Fig. 8e) than aloft (Fig.

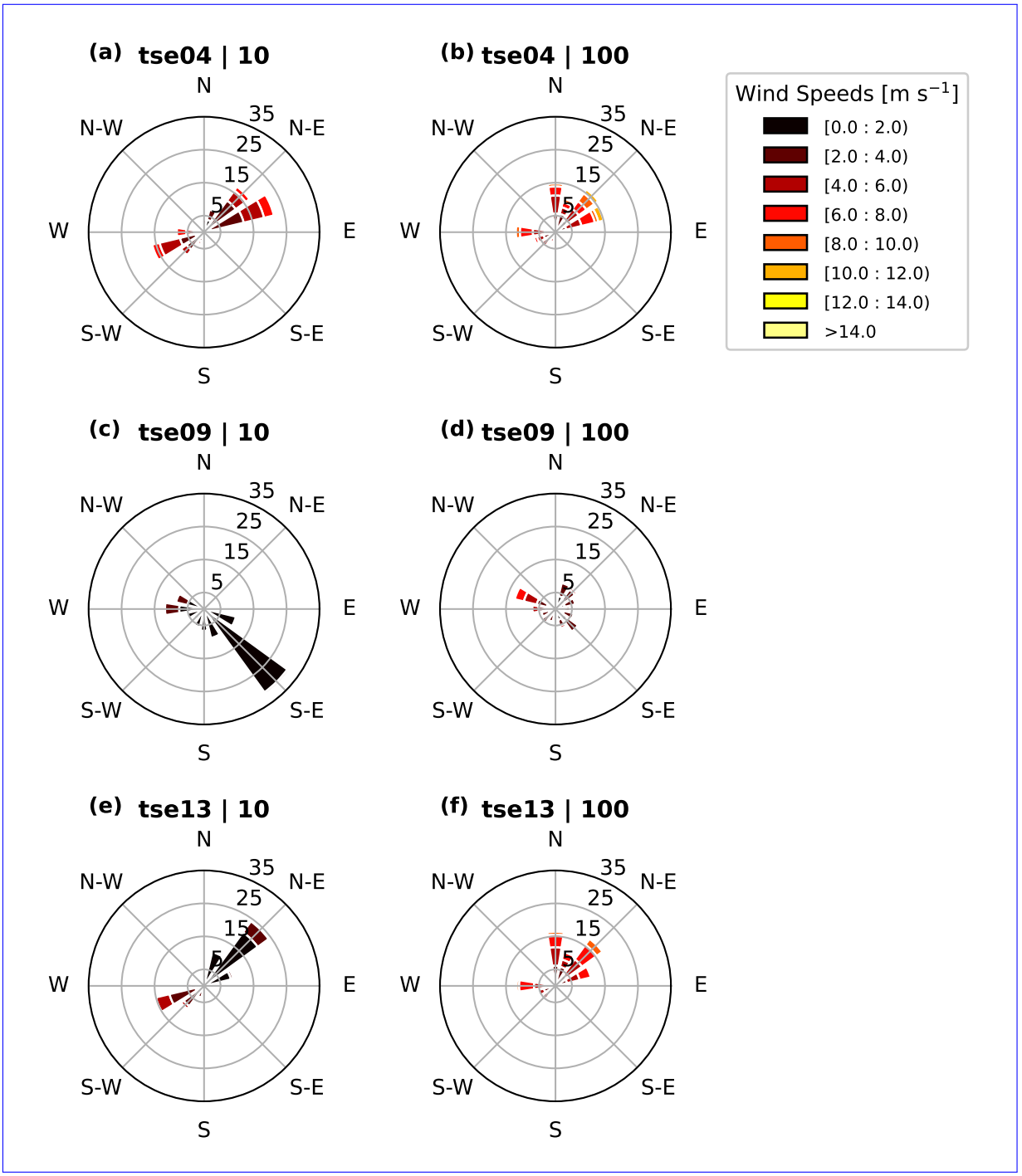

Figure 7. Perdigão (cloud removed) field campaign wind rose with 30 min averaging at the three 100 m towers and at 10 m (a, c, e) and 100 m (b, d, f) altitudes. The rings (i.e., 5, 15, 25, 35) correspond to the percentage of data that aligns with a given speed and direction. (a) tse04 (SW ridge) at 10 m; (b) tse04 (SW ridge) at 100 m; (c) tse09 (valley) at 10 m; (d) tse09 (valley) at 100 m; (e) tse13 (NE ridge) at 10 m; (f) tse13 (NE ridge) at 100 m.

8f) throughout all daytime hours, the L diurnal cycle on the SW ridge shows more similar frequencies of VU cases between the surface (Fig. 8a) and aloft (Fig. 8b) in the morning, with fewer VU cases at 100 m in the later afternoon. Of note, the SW ridge has ~~fewer~~ smaller percentage of VU cases than either the valley or the NE ridge.

The u_* diurnal cycle (Fig. 9) ~~explains~~ can explain the site-based differences in the reduction in VU contribution. u_* shows smaller values in the early morning (00–05 UTC) and evening (19–00 UTC) hours, with a shift toward larger values in the middle of the day (06–20 UTC) at all heights. The middle-of-day u_* in the valley also increases from 10 m measurements (Fig. 9c) to measurements at 100 m (Fig. 9d), suggesting an increased role of mechanical forcing and therefore a decreased role of buoyant forcing. This shift corresponds to a reduction in the representation of VU cases from the surface (Fig. 9c) to aloft (Fig. 9d). A similar trend exists at the NE ridge~~, although not as strong~~. Again, the middle-of-day u_* increase from the surface (Fig. 9e) to aloft (Fig. 9f) corresponds to a reduced contribution from VU cases. In contrast, the middle-of-day u_* at the SW ridge does not increase from the surface (Fig. 9a) to aloft (Fig. 9b) but actually slightly decreases. This middle-of-day u_* decrease from the surface to aloft along the SW ridge suggests a reduced role of mechanical forcing and therefore an increased role of buoyant forcing, thereby supporting the consistent number of VU cases between surface and aloft at the SW ridge in the morning hours (~~9–12~~ 09–12 UTC).

In contrast, the heat flux ($\overline{w't'_c}$) diurnal cycle (Fig. 10) ~~does not~~ cannot explain the reduced VU contribution aloft in the valley. The heat flux is smaller in the early morning (00–05 UTC) and evening (19–00 UTC) hours, with a shift and grows in the middle of the day (06–20 UTC). The midday maximum in heat flux along the two ridges is larger at the surface (Fig. 10a and e) than aloft (Fig. 10b and f). Further, in the valley, the midday heat flux maximum grows from the surface (Fig. 10c) to aloft (Fig. 10d).

Further, the u_* diurnal cycle appears regardless of the decomposition period. u_* is smallest during the morning hours (00–05 UTC), peaks in the middle of the day (06–20 UTC), and then drops again in the evening (21–24 UTC), regardless of the Reynolds decomposition period. During unstably stratified periods, u_* according to the 10 min Reynolds decomposition period is smaller than u_* based on a 30 min Reynolds decomposition period. This inability of the 10 min Reynolds decomposition period to resolve the full flux is most apparent at 10 m on the SW ridge (Fig. 11a).

The maximum u_* found in the stable periods of the u_* diurnal cycle also vary between the Reynolds decomposition periods. During these stable periods, the 30 min averaging approach yields the highest u_*, followed by the 10 min averaging approach. Again, this discrepancy at the surface is largest on the SW ridge (Fig. 11a). In contrast, the valley aloft (Fig. 11d) shows larger u_* differences based on the Reynolds decomposition period during stable periods than the two ridges (Fig. 11b, f).

The TKE diurnal cycle ~~also shows smaller values~~ is also smaller in the early morning (00–05 UTC) and evening (21–00 UTC) hours and grows in the middle of the day (06–20 UTC) (Fig. 12). While all three tower locations show larger values aloft (Fig. 12b, d, and f) than at the surface (Fig. 12a, c, and e), this trend is especially pronounced in the valley (Fig. 12b and c), perhaps due to advection of surface-generated turbulence from the ridges. Further, the valley shows a more muted diurnal cycle at 10 m (Fig. 12c) than the ridges show at 10 m (Fig. 12a and e).

The TKE diurnal cycle also emerges regardless of the decomposition approach, ~~although the~~ with a maximum value of TKE ~~is very~~ that is sensitive to the averaging period used. TKE is smaller during the early morning and evening hours and

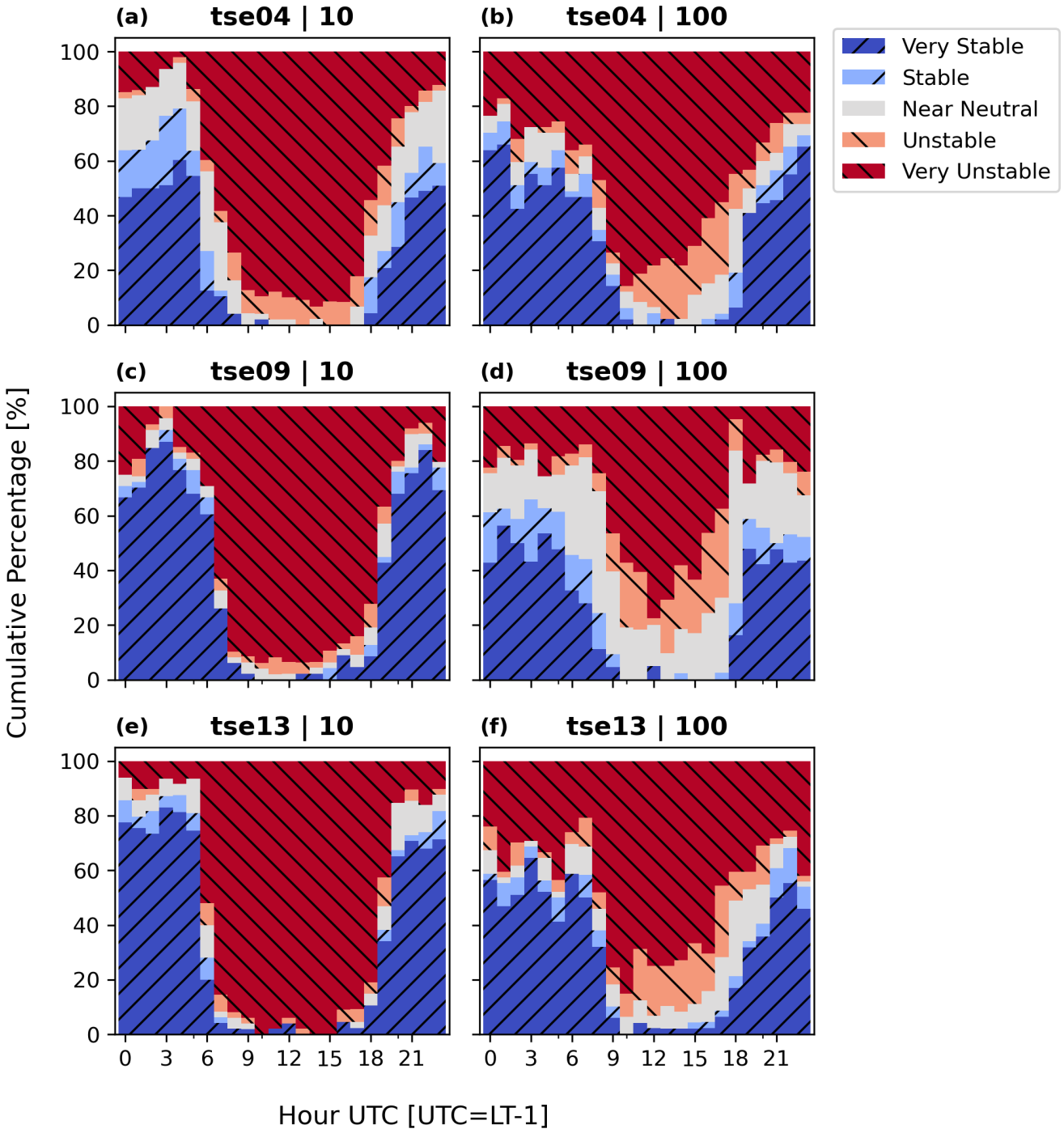

Figure 8. *L* diurnal cycle for ~~full~~ (cloud-removed) campaign period with 30 min averaging: (a) tse04 (SW ridge) at 10 m~~,~~; (b) tse04 (SW ridge) at 100 m~~,~~; (c) tse09 (valley) at 10 m~~,~~; (d) tse09 (valley) at 100 m~~,~~; (e) tse13 (NE ridge) at 10 m~~,~~; (f) tse13 (NE ridge) at 100 m.

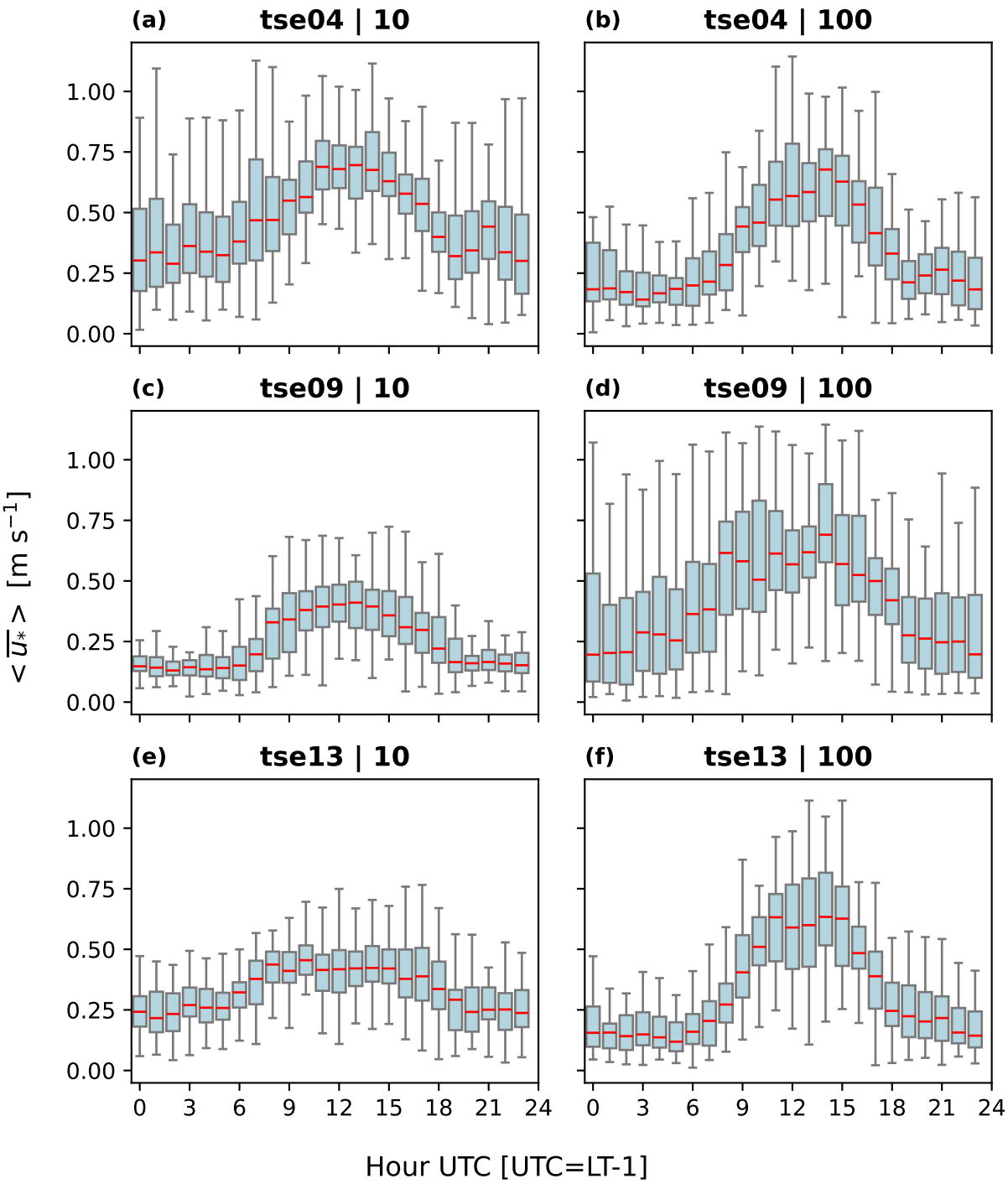

Figure 9. u_* diurnal cycle for ~~full~~ (cloud-removed) campaign period. Red lines indicate the median, and the box and whiskers are defined based on Q1 (25th percentile), Q3 (75th percentile), and the interquartile range (IQR) (Q3–Q1). The box encloses the IQR and the whiskers extend to $Q1 - 1.5 * IQR$ and $Q3 + 1.5 * IQR$. (a) tse04 (SW ridge) at 10 m~~,~~; (b) tse04 (SW ridge) at 100 m~~,~~; (c) tse09 (valley) at 10 m~~,~~; (d) tse09 (valley) at 100 m~~,~~; (e) tse13 (NE ridge) at 10 m~~,~~; (f) tse13 (NE ridge) at 100 m.

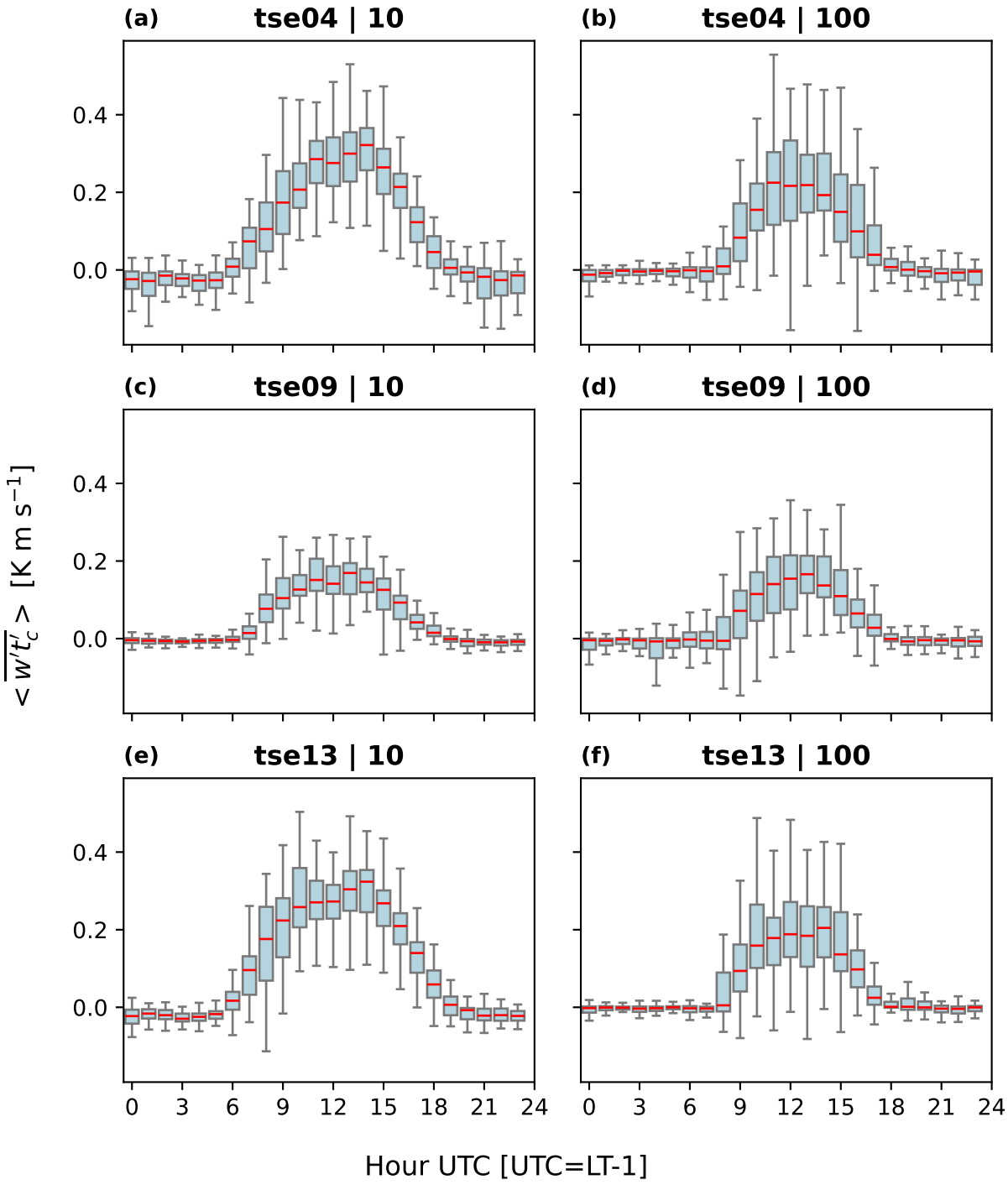

Figure 10. Heat flux diurnal cycle for ~~full~~ (cloud-removed) campaign period with 30 min averaging. Red lines indicate the median, and the box and whiskers are defined based on Q1 (25th percentile), Q3 (75th percentile), and the interquartile range (IQR) (Q3–Q1). The box encloses the IQR and the whiskers extend to $Q1 - 1.5 * IQR$ and $Q3 + 1.5 * IQR$. (a) tse04 (SW ridge) at 10 m~~,~~; (b) tse04 (SW ridge) at 100 m~~,~~; (c) tse09 (valley) at 10 m~~,~~; (d) tse09 (valley) at 100 m~~,~~; (e) tse13 (NE ridge) at 10 m~~,~~; (f) tse13 (NE ridge) at 100 m.

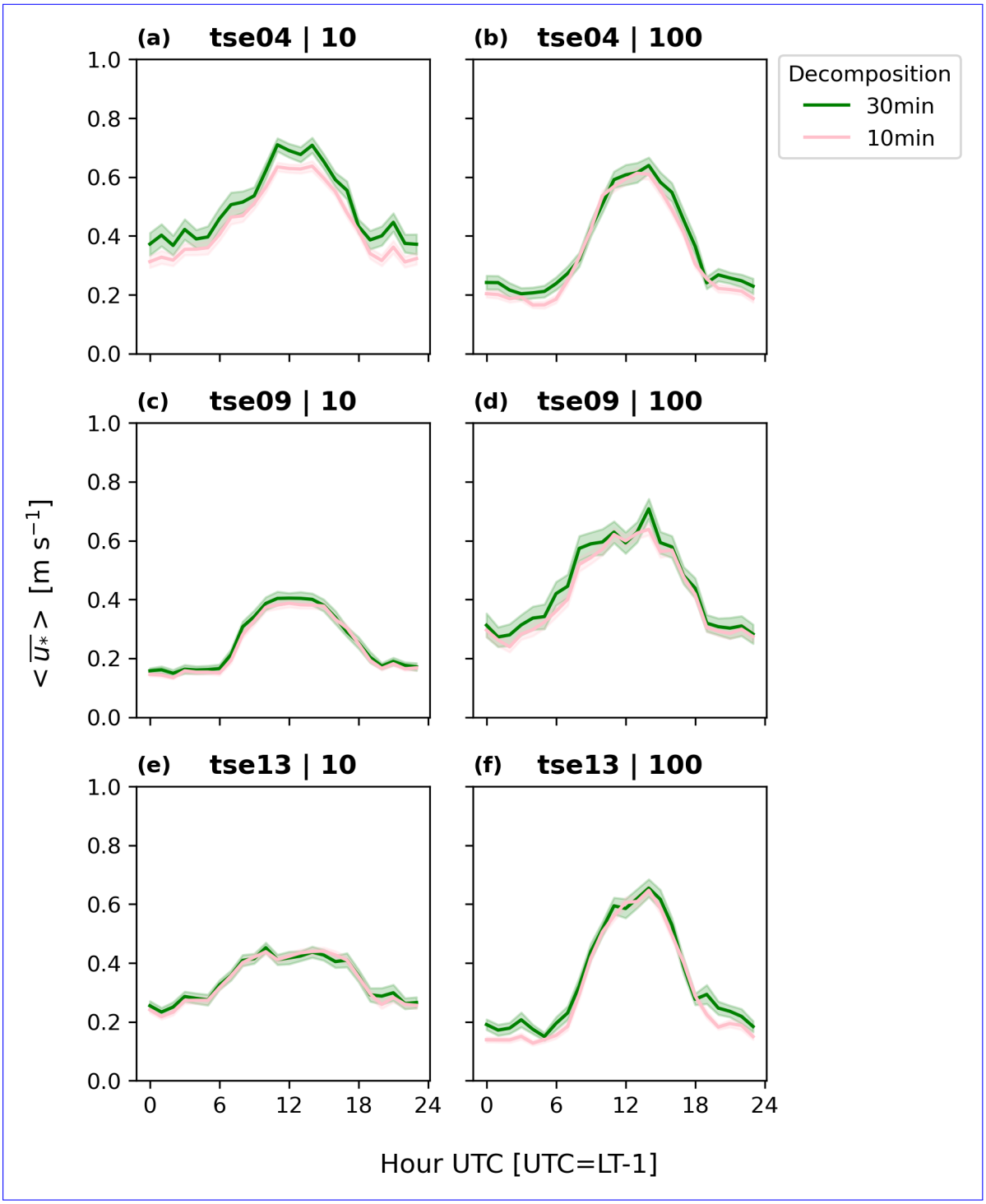

Figure 11. u_* diurnal cycle for ~~full~~ (cloud-removed) campaign period according to ~~three~~ two decomposition intervals. The solid line indicates the ~~median~~ mean value, and the band indicates the standard error. (a) tse04 (SW ridge) at 10 m~~,~~; (b) tse04 (SW ridge) at 100 m~~,~~; (c) tse09 (valley) at 10 m~~,~~; (d) tse09 (valley) at 100 m~~,~~; (e) tse13 (NE ridge) at 10 m~~,~~; (f) tse13 (NE ridge) at 100 m.

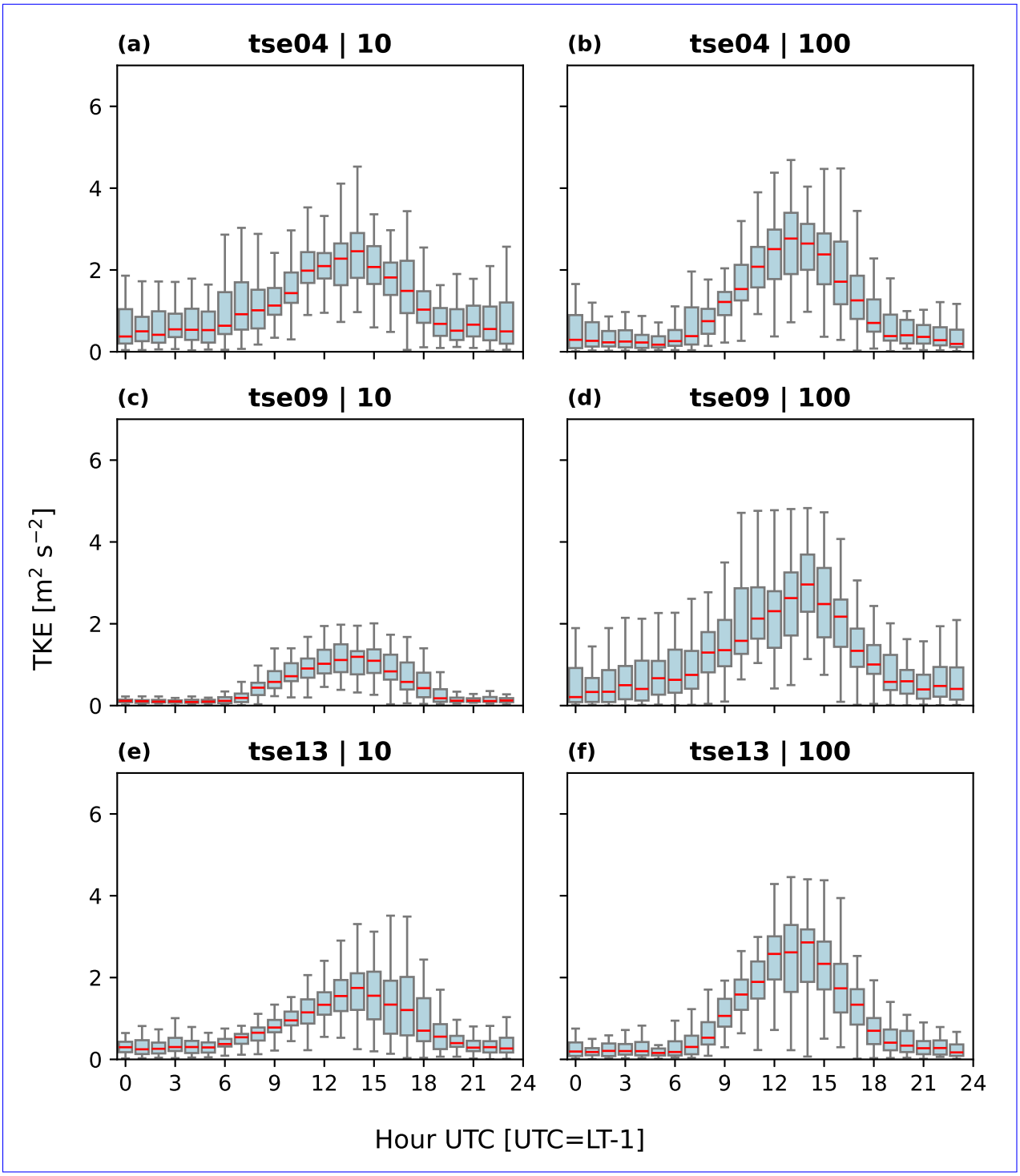

Figure 12. TKE diurnal cycle for ~~full~~ (cloud-removed) campaign period with 30 min averaging. Red lines indicate the median, and the box and whiskers are defined based on Q1 (25th percentile), Q3 (75th percentile), and the interquartile range (IQR) (Q3–Q1). The box encloses the IQR and the whiskers extend to $Q1 - 1.5 * IQR$ and $Q3 + 1.5 * IQR$. (a) tse04 (SW ridge) at 10 m~~,~~; (b) tse04 (SW ridge) at 100 m~~,~~; (c) tse09 (valley) at 10 m~~,~~; (d) tse09 (valley) at 100 m~~,~~; (e) tse13 (NE ridge) at 10 m~~,~~; (f) tse13 (NE ridge) at 100 m.

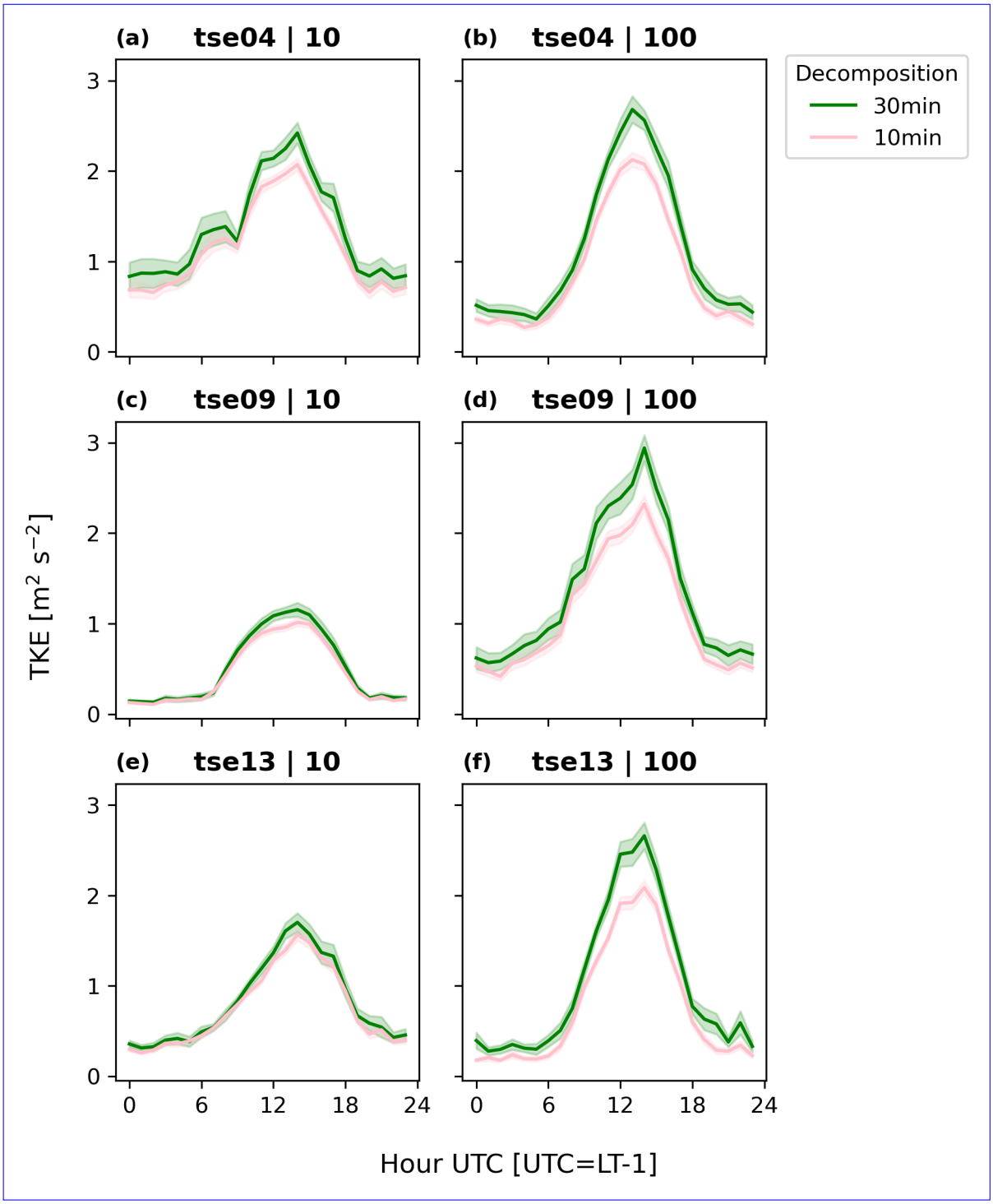

Figure 13. TKE diurnal cycle at three towers (tse04: a, b; tse09: c, d; tse13: e, f) for the ~~full~~ (cloud-removed) campaign period according to two averaging approaches at two heights (10 m: a, c, e; 100 m: b, d, f). The solid lines indicate the ~~median~~ mean value, and the bands indicate the standard error. (a) tse04 (SW ridge) at 10 m~~,~~; (b) tse04 (SW ridge) at 100 m~~,~~; (c) tse09 (valley) at 10 m~~,~~; (d) tse09 (valley) at 100 m~~,~~; (e) tse13 (NE ridge) at 10 m~~,~~; (f) tse13 (NE ridge) at 100 m.

grows in the middle of the day for all Reynolds decomposition windows, as was the case with u_* (Fig. 13) and as expected over land. Also consistent with the behavior observed with the u_* diurnal cycle, during ~~unstably~~ stably stratified periods, 30 min TKE and 10 min TKE are smaller (Fig. 13). ~~Further, this unstable~~ This stable period discrepancy based on the Reynolds decomposition window is ~~again most~~ pronounced at the surface only on the SW ridge (Fig. 13a) ~~and aloft in the valley~~ but for all locations aloft (Fig. 13~~d~~b,d,f). At the same time, the TKE diurnal cycle (Fig. 13) varies more during ~~stable~~ unstable periods based on the Reynolds decomposition window than the u_* diurnal cycle (Fig. 11). This spread based on the Reynolds decomposition window observed in the TKE emerges at both altitudes for all three towers (Fig. 13).

These trends in the TKE diurnal cycle also occur at intermediate heights (Fig. 14) with the largest differences at 10 m in the valley and on the canopied NE ridge. The TKE in the valley (Fig. 14c, d) shows stratified layers during nighttime hours, with smaller values at the surface and larger values with increasing height~~, suggesting decoupling or top-down boundary layer forcing.~~ .

One way to explain this apparent decoupling in the valley between the 10 m and 100 m measurements is to consider remote generation of turbulence that is then advected to the upper levels of the valley tower. This advection could occur horizontally, such that turbulence generated on the ridge is advected into the valley, where it is dissipated. This process could also occur vertically through the presence of an upside-down boundary layer (Parker and Raman, 1993; Mahrt, 1999). Warm air on the ridges may be advected over cold air pooled and trapped in the valley, leading to shear generation at the top of the cold pool (Mahrt, 1999). The explanation of an upside-down boundary layer in the valley is supported by a consistent TKE increase across intermediate heights between 10 m and 100 m within the valley (Fig. 14c, d), but not at the two ridge locations (Fig. 14a, b, e, f). This unique, well-mixed behavior during stable conditions in the valley is also reflected in the heat fluxes (Fig. 6e).

During the daytime period, the valley site shows stratification as well. This TKE stratification in the valley also persists for both Reynolds decomposition approaches. The 30 min valley TKE (Fig. 14c) differs most strongly between 10 m and 100 m, especially during the unstable middle of the day (Fig. 14d). The 10 min valley TKE (Fig. 14e) reduces the peak TKE and also reduces the gap between 10 m and 100 m TKE. The TKE ~~along the two ridges~~ on the NE ridge (Fig. ~~14a, b,~~ 14e,f) ~~does not show stratified layers. Rather, multiple levels frequently show the same value of TKE,suggesting well-mixed boundary layers~~reflects some of the same stratification as the valley (Fig. 14c,d), although the stratification on the NE ridge is less extreme. Further, ~~the~~ while the upper level TKE ~~along the SW ridge , with less vegetation~~ diurnal cycles are similar, the 10 m TKE remains separate on the NE ridge (Fig. ~~14a,b), is larger at the surface than aloft. In contrast,during the middle of the day, the NE~~ 14e,f), just as is observed in the valley (Fig. 14c,d). The TKE diurnal decoupling on the NE ridge is unique, however, in that the 10 m TKE pattern at this location increases at 18 UTC during the early evening transition while the 10 m TKE in the valley continues its decrease. The TKE diurnal cycle on the SW ridge (Fig. 14~~e,f) with extensive vegetation shows smaller~~ a,b) does not stratify into layers, regardless of the Reynolds decomposition window.

Canopy effects may help explain this 10 m TKE ~~at~~ decoupling during unstable conditions in the valley and NE ridge. These 10 m ~~than at upper levels.~~ measurements, located within the canopy layer but not necessarily within the vegetation layer, could experience heightened turbulence that would necessarily be reflected at taller measurements. Recirculation zones, also present during unstable conditions in the valley and NE ridge, may also influence this TKE decoupling. However, as noted in

Menke et al. (2019), the depth of these recirculation zones exceeds 100 m. Thus, because these recirculation zones would not necessarily impact 10 m measurements uniquely, their effect may be secondary to the more direct influence of the canopy.

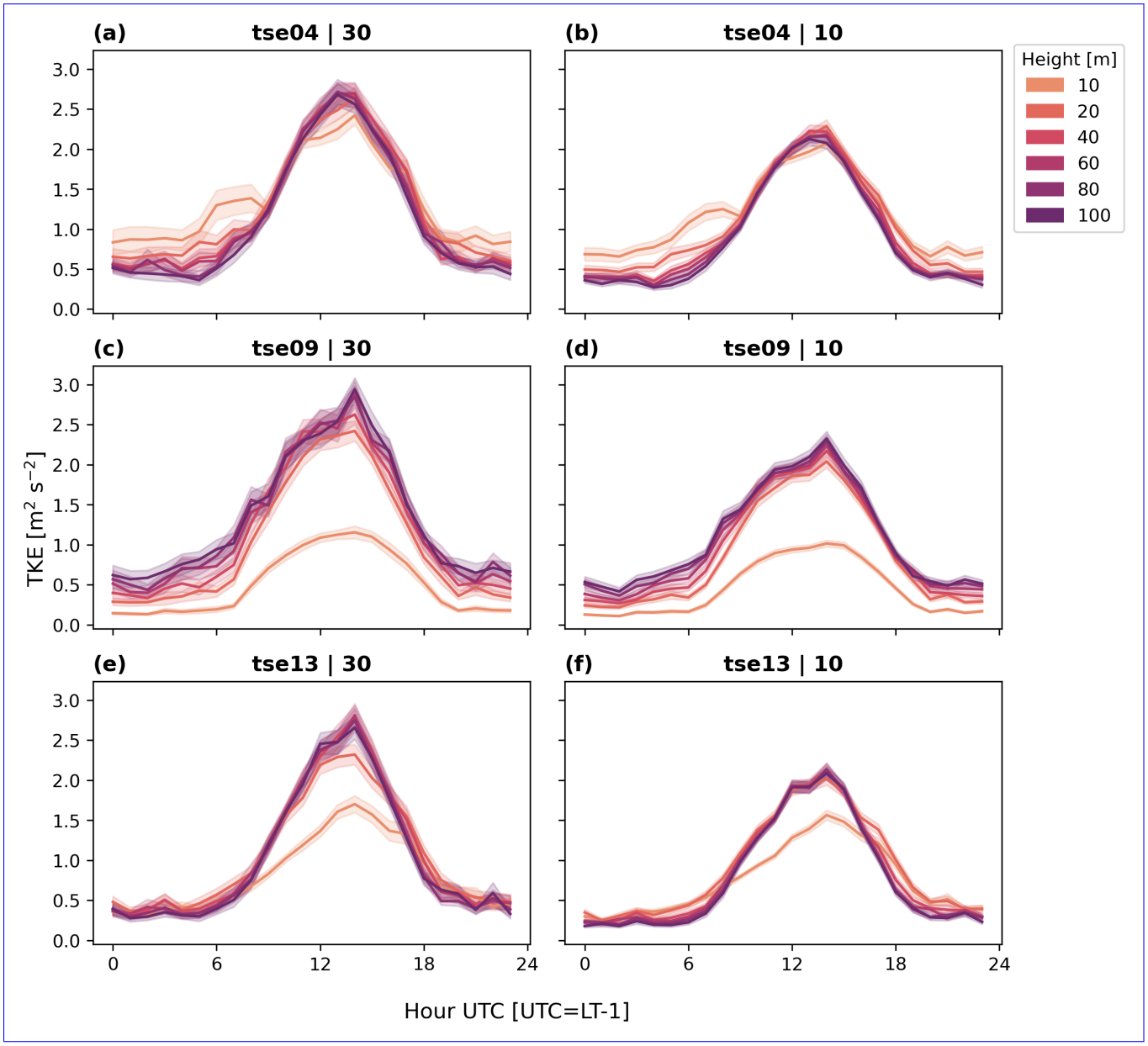

Figure 14. Diurnal cycle of TKE at all heights for each 100 m tower (tse04: a and b; tse09: c and d; tse13: g and h) according to two averaging approaches (30 min: a, c, e; 10 min: b, d, f). The solid line indicates the ~~median~~ mean value, and the band is the standard error. (a) tse04 (SW ridge) 30 min~~,~~; (b) tse04 (SW ridge) 10 min~~,~~; (c) tse09 (valley) 30 min~~,~~; (d) tse09 (valley) 10 min~~,~~; (e) tse13 (NE ridge) 30 min~~,~~; (f) tse13 (NE ridge) 10 min.

The ϵ diurnal cycle is the least pronounced of the three metrics considered (Fig. 15), which has implications for numerical modeling of flow in this complex terrain. While generally smaller values occur in the morning (00–05 UTC) and evening (21–00 UTC) hours and larger values in the middle of the day (06–20 UTC), the diurnal cycle is muted both at the surface on the NE ridge (Fig. 15e) and aloft in the valley (Fig. 15d). The ϵ diurnal cycle also differs between the ridges (Fig. 15a, b, e, and f) and the valley (Fig. 15c and d). While the two ridges show smaller ϵ values aloft (Fig. 15b and f) than at the surface (Fig. 15a and e) (opposite the TKE trends), the valley shows relatively consistent ϵ values between the surface (Fig. 15c) and aloft (Fig. 15d). The valley's larger values may again be due to advection of turbulence from the neighboring ridges, which must then dissipate in the valley. This local imbalance of dissipation rate, as seen also in Wildmann et al. (2019), has implications for numerical models that assume local balance between production and dissipation.

3.2 Stability metric analysis

3.2.1 Hub-height predictive index

Perdigão surface (10 m) measurements fail to represent conditions at turbine hub height (100 m). ~~All metrics show poor levels of HHPI at the surface.~~ The surface L rate of agreement is 50% or lower for all three towers (Fig. 16).~~The surface L HHPI also varies between towers, with higher HHPI on the two ridges than in the valley.~~

For TKE, surface HHPI is quantified by correlation and shows ~~a poor~~ poor and comparable R^2 for all tower locations~~with variability between towers. The TKE surface HHPI is highest on the NE ridge (0.618) (Fig. 16) and in the valley (0.616) (Fig. 16). The~~ . The SW ridge has a ~~lower~~ smaller TKE surface HHPI ~~of 0.509~~ (Fig. 16).

The ϵ surface HHPI also shows very poor performance (Fig. 16) with R^2 values always less than ~~0.4~~0.3 and especially poor on the NE ridge. This consistently ~~low~~ poor surface HHPI leaves ϵ as the worst metric to make hub-height predictions based on surface measurements. ~~ϵ surface HHPI also reflects ridge/valley distinctions with higher surface HHPI along the two ridges~~ Measurements at higher altitudes lead to larger HHPI for all metrics (Fig.~~16a, c)than in the valley (Fig. 16b).~~

~~Higher locations on the towers lead to higher HHPI~~ 16). The overall L HHPI profile shows negligible variability based on tower. Each tower begins with an L HHPI of approximately 0.4-0.5 and steadily increases to an L HHPI of approximately 0.6-0.7, regardless of the tower location (Fig. 16a,b,c). The TKE HHPI profile ~~on the SW ridge~~ consistently shows larger HHPI than the other two metrics overall, regardless of the location (Fig. 16a~~) improves agreement with the 100 m measurement as measurements move up. The~~ ,b,c). Further, while the TKE HHPI ~~profiles in~~ increase is consistent within the valley (Fig. 16b)~~and on the NE ridge~~ , this increase is more discontinuous along the two ridges (Fig. 16~~c) consistently improve hub-height agreement with higher observations~~a,c). The ϵ HHPI profile shows the ~~most consistent~~ largest increase across heights as well as the greatest consistency across tower locations. Although the ϵ HHPI (Fig. 16) at the surface is the lowest of the three metrics, the ϵ HHPI (Fig. 16) steadily increases to (slightly) overtake the L HHPI (Fig. 16) at all three sites ~~.~~ (Fig. 16a,b,c).

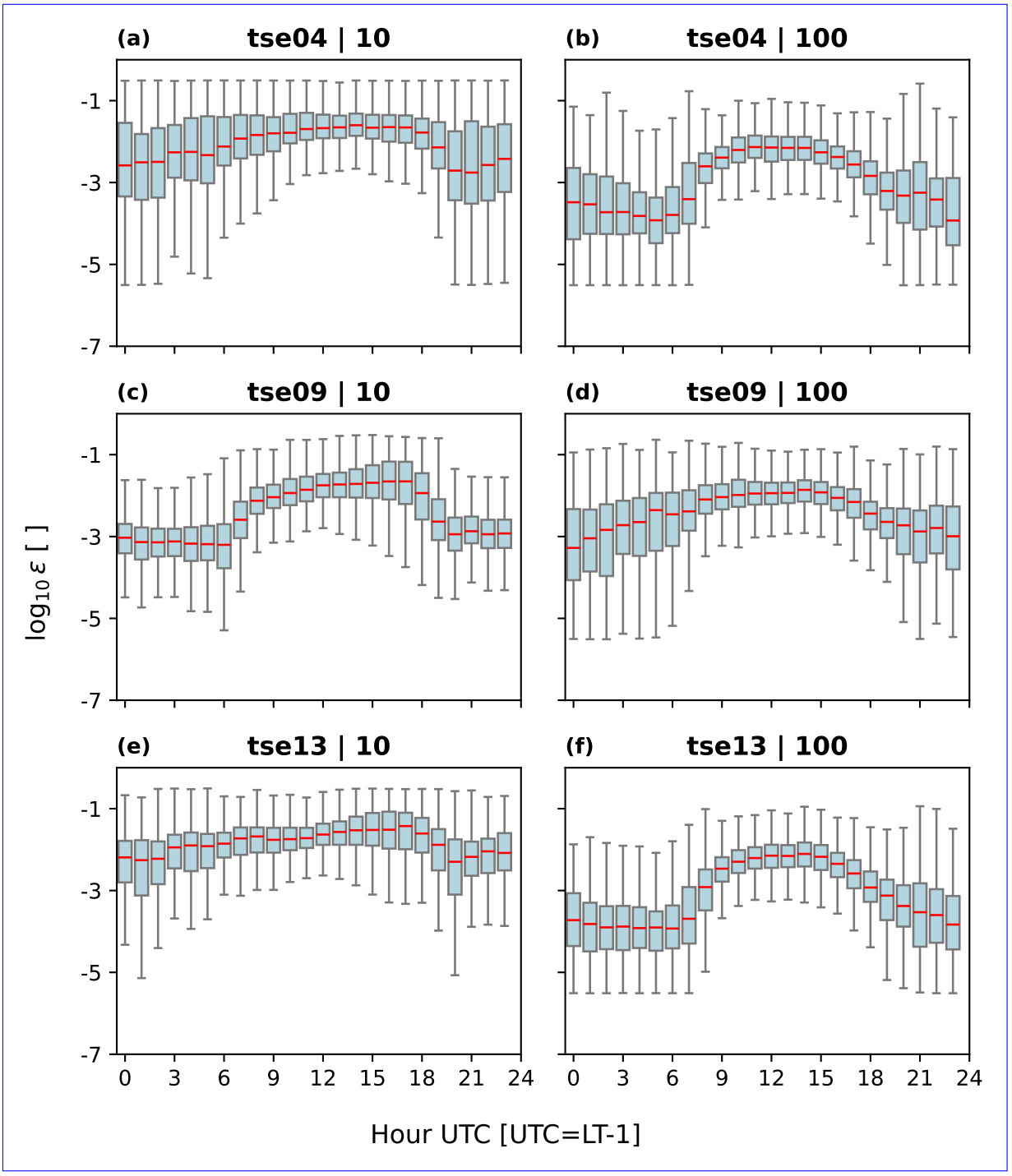

Figure 15. ϵ diurnal cycle for ~~full~~ (cloud-removed) campaign period. Red lines indicate the median, and the box and whiskers are defined based on Q1 (25th percentile), Q3 (75th percentile), and the IQR (Q3–Q1). The box encloses the IQR and the whiskers extend to $Q1 - 1.5 * IQR$ and $Q3 + 1.5 * IQR$. (a) tse04 (SW ridge) at 10 m~~,~~; (b) tse04 (SW ridge) at 100 m~~,~~; (c) tse09 (valley) at 10 m~~,~~; (d) tse09 (valley) at 100 m~~,~~; (e) tse13 (NE ridge) at 10 m~~,~~; (f) tse13 (NE ridge) at 100 m.

~~Correlation coefficient between the base height and 100 m for full campaign period with 30 min averaging. (a) tse04 (SW ridge), (b) tse09 (valley), (c) tse13 (NE ridge). tse13 60 m L calculations were omitted due to high (76%) temperature data unavailability.~~

~~HHPI is negligibly affected~~ The valley is the site with HHPI most impacted by the Reynolds decomposition ~~period. While assessments like the L HHPI on the SW ridge~~ window. All three sites experience HHPI improvements with a longer averaging window,corroborating the role of the enhanced TKE characterization. However,these performance improvements are negligible along the two ridges (Fig.~~17a) and~~ 17a,b,g,h). In contrast, the TKE HHPI ~~both on the SW ridge~~ in the valley maintains an approximately 0.1 improvement at low altitudes with the longer window (Fig.~~17d)and~~ 17b). This performance improvement with a longer window in the valley further corroborates the already-noted TKE stratification in the valley (Fig.~~17e) suggest slight differences between Reynolds decomposition periods,these differences are both subtle and unsustained at all tower measurement heights. This lack of performance difference~~ 14c,d).

The otherwise consistent performance between the 10 min and 30 min Reynolds decomposition windows does not necessarily suggest that 10 min Reynolds decomposition windows and 30 min Reynolds decomposition windows resolve similar fluxes. In fact, several analyses in this work, including ~~ogives~~ CFAW-CM (Fig.~~4~~ 4 and Fig. 5) and diurnal cycles (Fig. 8–Fig. 15), suggest otherwise. Rather, because the HHPI assessment compares stability metrics with the same Reynolds decomposition window, the relative lack of performance improvement with a 30 min Reynolds decomposition window may instead suggest that a longer Reynolds decomposition window may not be an appropriate alternative to building taller towers.

3.2.2 Horizontal homogeneity

We sought to define the minimum number of towers to represent the variability in the 10 m measurements at Perdigão using the Louvain community detection algorithm. A ~~nine-tower~~ nine tower subset spans all groupings across all metrics (Fig. 18). While this subset is not the only potential subset that spans all groupings across all metrics, this tower subset indicates the smallest number of towers necessary to fully characterize the site's partitions in TKE, L, and ϵ for either Reynolds decomposition window considered here.

The towers cluster into groups that generally follow terrain boundaries~~(Fig. 18).~~ . For example, with a 30 min averaging period, the L groupings ~~(Fig. 18a) define the SW (purple~~define a SW ridge (orange) and NE ~~(orange) ridges, respectively, with the exception of the forest green rne02 (Fig. 18a). The ridge partitions are also influenced by two transect (brown and light green) partitions (Fig. 18a). In between the ridge partitions and the transect groupings lies a valley partition (Fig. 18a, dark blue) and a valley pocket~~ ridge (blue) as well as dark blue and yellow transects. These dark blue and yellow transects are also separated by a valley that is defined by both blue and lavender pockets (Fig. 18a~~, lavender~~). Similar ~~terrain patterns are~~ partitions are also reflected in the ~~10 min L groupings (Fig. 18b), the TKE (Fig. 18c, d) groupings, and the~~ and ϵ groupings (Fig. 18~~e,f)groupings~~c,e).

The TKE ~~groupings~~ and ϵ groupings also differ from ~~the~~ those presented with L~~groupings. While the L groupings treat rne02 (Fig. 18a , forest green) as its own partition, the~~ . Both TKE ~~groupings~~ and ϵ present a more mixed transect as opposed to a single transect (Fig. 18c~~) see this tower as part of the NE ridge (orange),and the~~ ,e). TKE and ϵ groupings ~~(Fig. 18e) instead~~

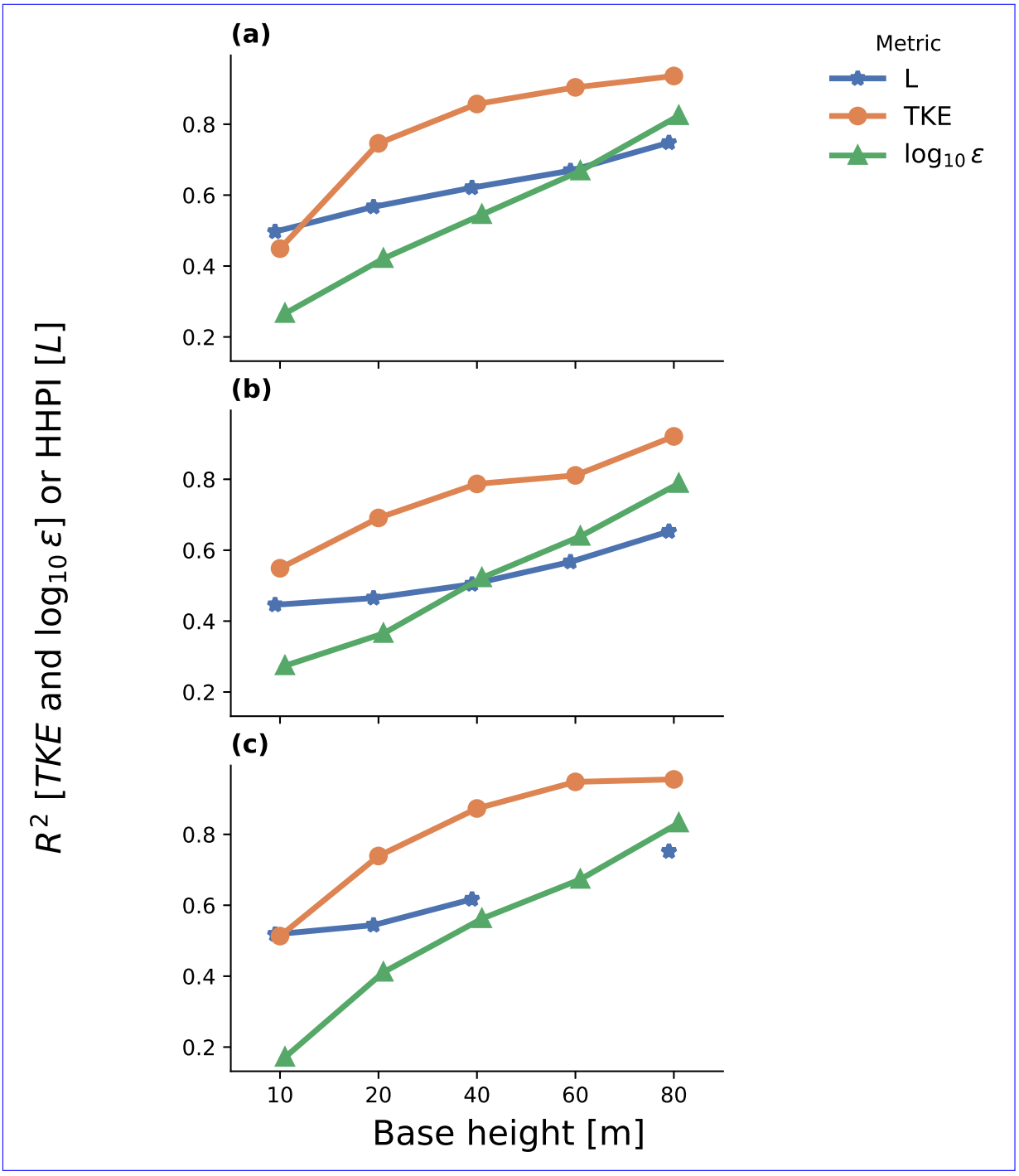

Figure 16. Correlation coefficient between the base height and 100 m for ~~full~~ (cloud-removed) campaign period ~~according to two~~ with 30 min averaging~~approaches~~. ~~In all cases, ϵ~~ tse13 60 m L calculations ~~are maintained at their 30 s resolution~~were omitted due to high (76%) temperature data unavailability. (a) tse04 (SW ridge)~~L, ;~~ (b) ~~tse04 (SW ridge) TKE, (c) tse04 (SW ridge) ϵ, (d)~~ tse09 (valley)~~L, ;~~ (~~e~~c) ~~tse09 (valley) TKE, (f) tse09 (valley) ϵ, (g)~~ tse13 (NE ridge)~~L, (h) tse13 (NE ridge) TKE, (i) tse13 (NE ridge) ϵ~~.

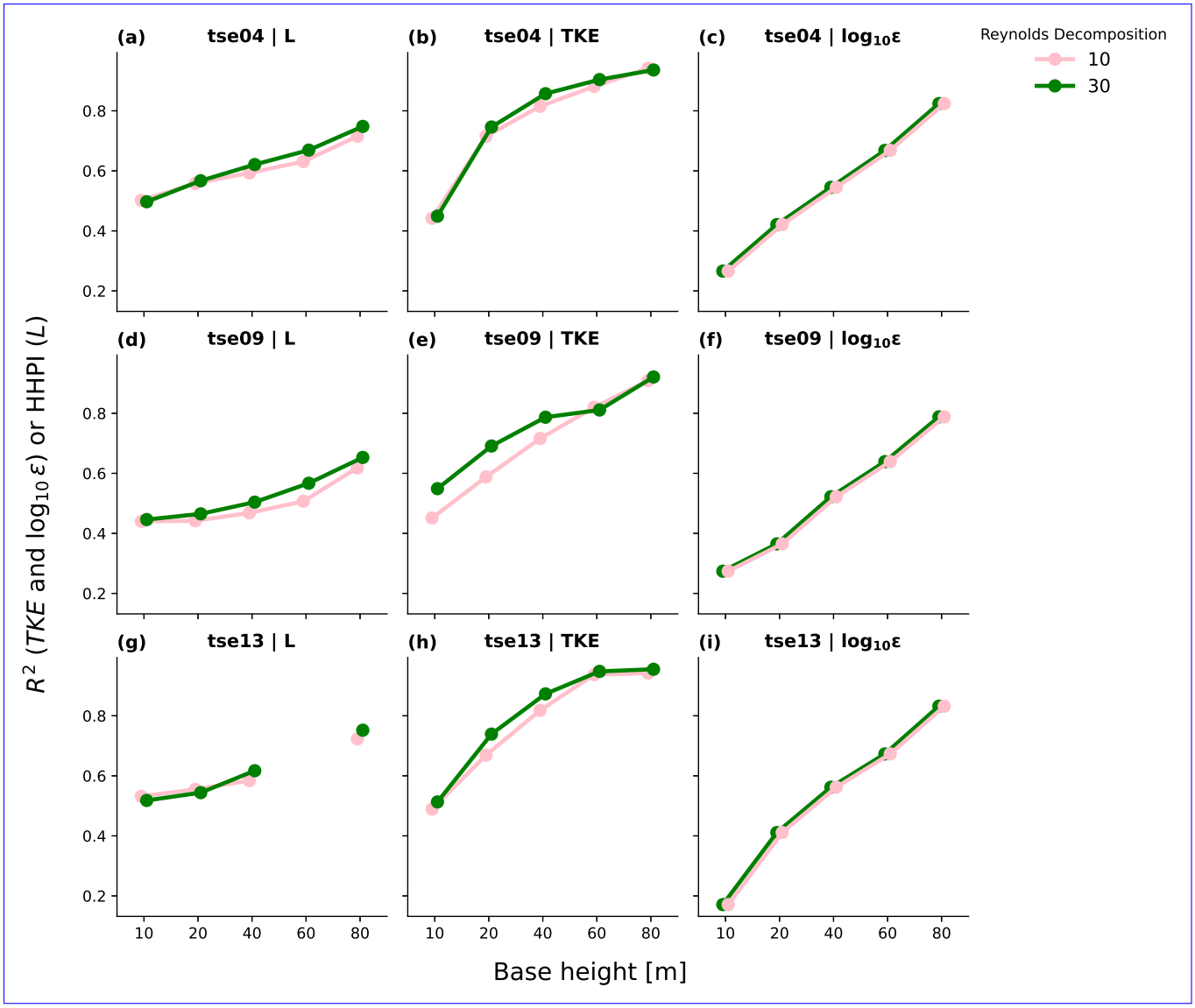

Figure 17. Correlation coefficient between the base height and 100 m for (cloud-removed) campaign period according to two averaging approaches. In all cases, ϵ calculations are maintained at their 30 s resolution. (a) tse04 (SW ridge) L; (b) tse04 (SW ridge) TKE; (c) tse04 (SW ridge) ϵ; (d) tse09 (valley) L; (e) tse09 (valley) TKE; (f) tse09 (valley) ϵ; (g) tse13 (NE ridge) L; (h) tse13 (NE ridge) TKE; (i) tse13 (NE ridge) ϵ.

~~treat the tower as an extension of the SW ridge (purple). The TKE groupings (~~also see the NW transect as distinct from the SE transect (Fig. 18c~~) also suggest a new (turquoise) partition outside of the SW ridge that neither the L~~ ,e). ϵ groupings also notably are the least able to differentiate between the wo ridges themselves (Fig. 18~~a)~~nor the e). The ϵ groupings also suggest a fairly uniform valley (Fig. 18e)~~acknowledge. Finally, the~~ , while both TKE ~~groupings and the ϵ groupings differ in their characterization of tse08. The TKE groupings treat tse08~~ (Fig. 18c~~, middle purple) as an extension of the SW ridge while the ϵ groupings absorb tse08 into the valley (Fig. 18e, dark blue). The~~) and L ~~characterization of this tower is different still, treating this tower as an extension of the outside (brown) transect (~~(Fig. 18a) suggest greater variability within the valley.

The Reynolds decomposition window ~~shifts the placement – but not the number – of partitionsfor a given metric. Seven~~ also shifts partitions. Both tnw08 and tse08 shift for both L ~~groupings exist, regardless of whether a~~ and TKE between 30 min ~~(Fig. 18a) or~~ and 10 min~~(Fig. 18b) Reynolds decomposition window is employed. However, the L groupings~~ . tnw08 shifts from dark blue to turquoise as a distinct partition for both metrics. tse08 also shifts based on the averaging window. For TKE tse08 is seen as a SW ridge (orange) tower with a 30 min ~~Reynolds decomposition window (Fig. 18a) treat rne02 (dark green) as its own partition while the L groupings~~ averaging window but as an independent (grey) tower with a 10 min Reynolds decomposition~~window (Fig. 18b) treat rne02 as part of the NE ridge. The L groupings with the 10 min~~ . Clearly, tse08 represents a divide within the valley.

We also see cases where the Reynolds decomposition window ~~(Fig. 18b) also treat tse08 (light blue) as its own partition while the~~ shifts the partition for one metric but not another. rne02 shifts an L ~~groupings with the 30 min Reynolds decomposition windowtreat tse08 as~~ partition from (relatively unique) pink to being misattributed as a SW ridge tower with a 10 min averaging window. Similarly, tnw04 is determined to be part of the ~~(brown) transect grouping. The L grouping with the~~ SW transect (dark blue) for 30 min ~~Reynolds decomposition window (Fig. 18a) also treats v01 (lavender) as its own partition while the L groupings with the~~ TKE and is more appropriately absorbed with 10 min ~~Reynolds decomposition window treat v01 as an extension of the (light green) transect grouping. The net result of these shifts in partition placement is that the same number of towers is necessary to characterize L for a given Reynolds decomposition window, but two additional towers are necessary to capture the variability between metrics. The~~ as a mid-blue. This sensitivity in the valley to the Reynolds decomposition window~~also shifts the placement of the five~~ , especially for TKE~~partitions. Tower tse08~~ , is consistent with many results presented in this work (Fig. ~~18c,middle purple) is treated as an extension of the SW ridge with a 30 min Reynolds decomposition window and part of the valley with a 10 min Reynolds decomposition window.~~ 14c,d and Fig. 17d,e and Fig. 13c,d).

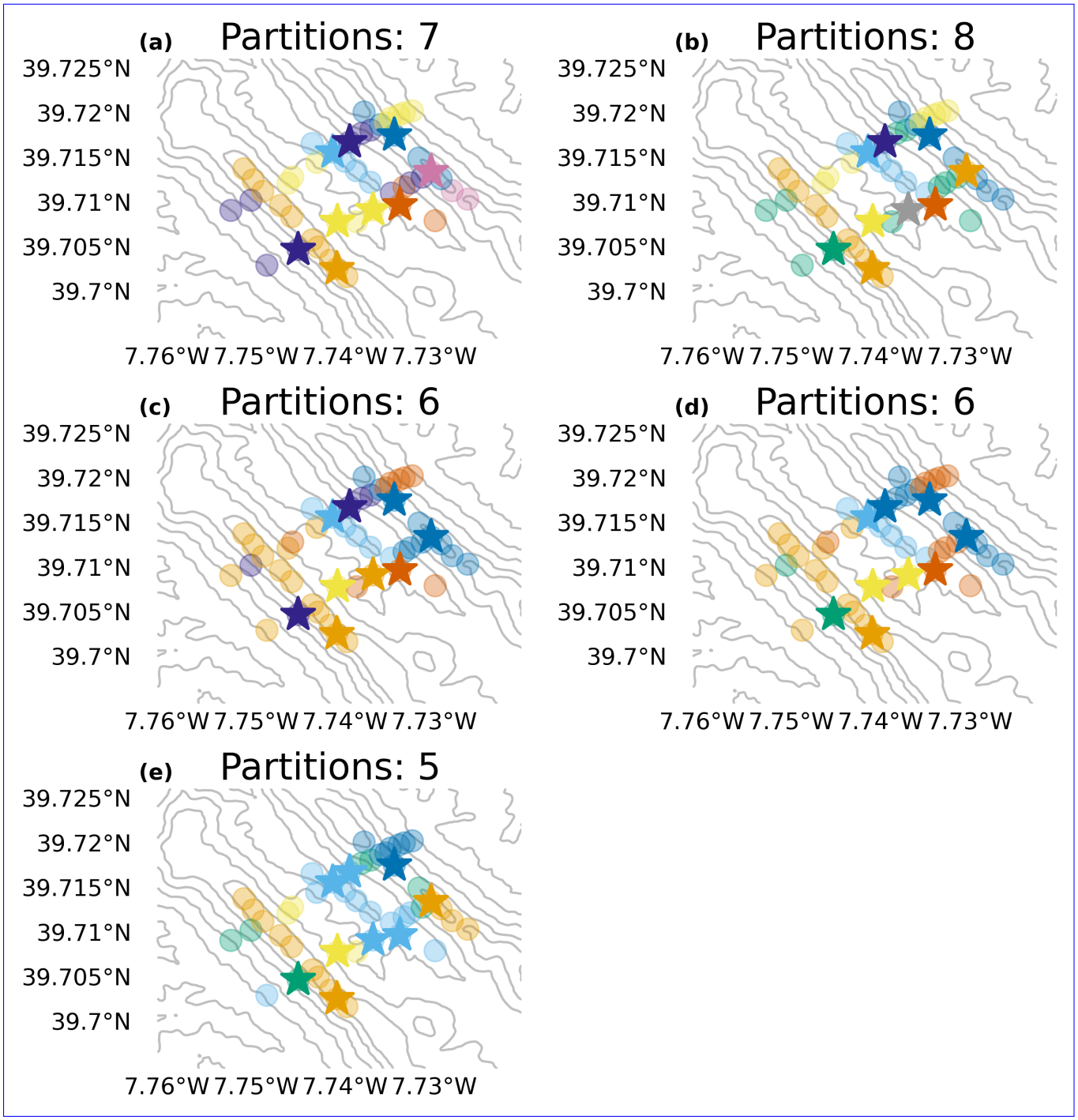

Figure 18. Groupings determined by the Louvain community detection algorithm for each metric. The number of colors corresponds to the number of tower groupings, and towers of the same color correspond to the same tower grouping. A nine-tower subset indicated with stars spans all groupings across all metrics. (a) L 30 min; (b) L 10 min; (c) TKE 30 min; (d) TKE 10 min; (e) ϵ 30 s.

4 Discussion

Stability metrics are ~~determined by~~ sensitive to the Reynolds decomposition window used to calculate them. Wind energy industry approaches have historically relied on a consistent 10 min averaging period, regardless of the stability regime (IEC; Bailey et al., 1997; Goit et al., 2022). This 10 min Reynolds decomposition window assumes (or potentially mis-assumes) clear separation between the large-scale mesoscale motions and the small-scale turbulent motions and that the 10 min Reynolds decomposition window appropriately distinguishes both regimes. In contrast, a longer, 30 min, Reynolds decomposition window has the potential to resolve more turbulent fluctuations while still avoiding larger-scale mesoscale motions. This difference is clearly seen in the maximum TKE values during the middle of the day (Figs. 13, 14) where the 30 min window can include ~~circulations that fill~~ the turbulent circulations that span the deeper daytime convective boundary layer.

The Reynolds decomposition window impacts turbulence characterization on the SW ridge. Notably, 10 m TKE differences between Reynolds decomposition windows are larger at the SW ridge (Fig. 13a) than in the valley (Fig. 13c) or on the NE ridge (Fig. 13e), both during stable and unstable periods. The same is true for the u_* diurnal cycle (Fig. 11). Similarly, the u_* ~~ogive~~ CFAW-CM analysis on the SW ridge reflects anomalous behavior during ~~stable~~ unstable periods in which a 30 min averaging period is not sufficiently long (Fig. 5).

The Reynolds decomposition window also impacts stability characterization in the valley. The L and TKE partitions in the valley shift depending on whether a 30 min (Fig. 18a) or 10 min Reynolds decomposition window is used during stable periods (Fig. 18b, c). Similarly, the strength of TKE stratification is also influenced by the Reynolds decomposition window ~~.~~

~~One way to explain this apparent decoupling~~ (Fig. 14). This more complete characterization of the TKE stratification in the valley ~~between the~~ with a 30 min Reynolds decomposition window over a 10 ~~m and 100 m measurements is to consider remote generation of turbulence that is then advected to the upper levels of the valleytower. This advection could occur horizontally, such that turbulence generated on the ridge is advected into the valley, where it is dissipated. This process could also occur vertically through the presence of an upside-down boundary layer (Parker and Raman, 1993; Mahrt, 1999). Warm air on the ridges may be advected over cold air pooled and trapped in the valley, leading to shear generation at the top of the cold pool (Mahrt, 1999). The explanation of an upside-down boundary layer~~ min Reynolds decomposition window also translates to an improved TKE HHPI in the valley. Thus, employing the CFAW-CM to determine an optimal (potentially longer) averaging window can improve atmospheric stability characterization.

Increasing the length of the Reynolds decomposition window, however, does not necessarily improve the HHPI for any metrics or locations outside of TKE in the valley~~is supported by a consistent TKE increase across intermediate heights between 10 m and 100 m within the valley (Fig. 14c, d), but not at the two ridge locations (Fig. 14a , b, e, f)~~. This general lack of HHPI improvements with a longer Reynolds decomposition window does not necessarily suggest that the fluxes are the same. Rather, this general lack of HHPI improvement suggests that a longer Reynolds decomposition window may not be a suitable alternative to building taller towers.

~~Regardless of the location or the exact mechanism, the overall low~~ The overall small surface HHPI values have potential implications for the utility of shorter towers when information at 100 m is needed. The ~~low~~ small HHPI values (Fig. 16) suggest

that surface measurements are unable to make hub-height predictions, regardless of the Reynolds decomposition window. Thus, meteorologists may not be able to avoid investing in hub-height-tall meteorological towers to make informed hub-height predictions.

The HoH results also have potential implications for those who need information over a broad area in complex terrain. Results from the Louvain community detection algorithm analysis of the observations suggest shared behavior among towers in common terrain (Fig. 18). Thus, complex terrain meteorologists may be able to reduce the number of towers necessary to understand surface stability by strategically placing tower locations in areas of differing terrain. Researchers and developers may also consider implementing the Louvain community detection algorithm with flow models such as large-eddy simulations ~~(Wise et al., 2021)~~ like those in Wagner et al. (2019), Wise et al. (2021), Robey and Lundquist (2024), and Giani and Crippa (2024) (among others) to assess locations required for tower siting. Appendix C includes an proof-of-concept application of the Louvain community detection algorithm to a short-duration large-eddy simulation.

5 Conclusion

Characterizing atmospheric stability is crucial for multiple wind energy applications and becomes more challenging in heterogeneous complex terrain. This work ~~improves~~ demonstrates the challenges in atmospheric stability characterization in complex terrain by analyzing how atmospheric stability varies in the Perdigão valley. We assess the utility of building taller towers at three strategic locations and also consider the optimal tower number and placement to sample variability in the atmospheric stability for the complex site. We perform these assessments based on three stability metrics~~—~~: the Obukhov Length (L), the turbulence kinetic energy (TKE), and the turbulence dissipation rate (ϵ). We also repeat these assessments according to different Reynolds decomposition windows, considering a consistent 30 min averaging window common in the atmospheric science community and a consistent 10 min averaging that is standard in the wind energy community.

Results provide potentially valuable insights for those interested in analyzing areas of complex terrain. For example, 10 m surface measurements do not provide reliable 100 m hub-height stability predictions. Thus, it may be necessary to invest in meteorological towers that extend to hub height to make effective hub-height predictions.

Results here also provide insights regarding approaches to defining the number and location of meteorological towers necessary to accurately characterize a complex terrain site, at least in terms of atmospheric stability parameters such as TKE, ϵ, and L. Different results ~~make~~ occur from variations in wind speed, wind direction, and/or turbulence intensity. Specifically, ~~results from this analysis suggest~~ this analysis suggests that it may be possible to reduce the number of necessary meteorological towers by strategically sampling towers in regions of differing terrain and by coupling community detection algorithms with flow models like those in Wise et al. (2021), Robey and Lundquist (2024), and Giani and Crippa (2024), among others.

Results also reflect how atmospheric stability characterizations are influenced by choices in the Reynolds decomposition window. The Reynolds decomposition window influences stability characterization in the valley, such that a 30 min Reynolds decomposition window during unstable periods better captures maximum values, and during stable periods clarifies the TKE stratification in this location. Collectively, the results presented herein speak to the challenges that ~~stakeholders and~~

~~meteorologists~~ meteorologists and other analysts may face in balancing the need for accurate characterizations of atmospheric stability in areas of complex terrain with the financial implications of investing in ~~expensive~~ meteorological towers.

These results also ~~open up~~ suggest opportunities for future work that could inform improved characterization of atmospheric stability in complex terrain. ~~For example, an application of the Louvain community detection algorithm to large-eddy simulations (Wise et al., 2021) for the Perdigão site could demonstrate the effectiveness of this approach for identifying critical locations for measurements. Such a tool could streamline future field experiment or wind resource assessment campaigns, or the design of mesonets (Brock et al., 1995; Brotzge et al., 2020).~~

~~Finally, future work may also~~ Future work could involve extending the assessments presented in this analysis to other sites with complex terrain and with more stability metrics. For example, analyzing heavily vegetated sites and sites over water could improve understanding of surface roughness length variability and the corresponding similarity relationships. Further, introducing more stability metrics could support ~~stakeholders and meteorologists evaluating~~ evaluations of the relative value of investing in more sensors to calculate an Obukhov ~~length~~ Length as opposed to more cost-effective stability characterizations (Cantero et al., 2022).

Code and data availability. The Perdigão tower data can be found at: https://data.eol.ucar.edu/dataset/536.011 . The processing code can be found at: [Insert upon acceptance]. The XPIA tower data can be found at: [Insert upon acceptance]. The XPIA sonic data can be found at: [Insert upon acceptance]. The processed data can be found at:[Insert upon acceptance]. <A GitHub repository will be made available upon acceptance.>

Appendix A

Table A1. Dates included (i.e. not flagged according to the Supplement to Fernando et al. (2019) as presenting low clouds, middle clouds, thunderstorms, or fog) in analysis.

Date0.5ex>0.5ex
01 May
02 May
03 May
07 May
15 May
16 May
18 May
19 May
20 May
21 May
23 May
30 May
31 May
01 June
03 June
04 June
05 June
07 June
08 June
09 June
10 June
11 June
12 June
13 June
14 June1ex>1ex

Appendix B

Here we provide a flat terrain comparison to the Perdigão HHPI analysis. This flat terrain benchmark serves to contextualize the role of complex terrain in affecting the relative agreement between surface and hub-height stability. Sonic anemometer data from the Boulder Atmospheric Observatory (BAO) tower during the three-month eXperimental Planetary boundary layer Instrumentation Assessment (XPIA) (Lundquist et al., 2017; Bodini et al., 2018) field campaign provide the data source for this comparison. Available measurements include data from 5m, 50m, and 100m. As such, we compare both the 5 m - 100 m and 50 m - 100 m. Each stability metric calculation employs a screening process similar to that employed for the Perdigão data, including removal of the approximately 20% of data affected by precipitation, 99.5th percentile extrema removal, and tower wake distortion screening.

HHPI is higher in flat terrain than in complex terrain at shorter heights. HHPI in flat terrain is similar to HHPI in complex terrain in several ways. Both improve with taller towers. In both cases, $\log_{10}\epsilon$ has the lowest HHPI of all metrics and this metric distinction is especially-pronounced for shorter heights (Fig. B1c). Both terrains also exhibit similar curvatures for each metric. L HHPI consistently is flatter at lower heights, and increases more sharply at higher heights (Fig. B1a). TKE HHPI increases more sharply for shorter heights before increasing more gradually above (Fig. B1b). $\log_{10}\epsilon$ HHPI is unique in its consistent linear increase (Fig. B1). HHPI in the two terrains also differ. Notably, HHPI is higher in flat terrain than in complex terrain (Fig. B1). Surface L HHPI is between 0.1 and 0.2 higher in flat terrain than in complex terrain (Fig. B1a). Surface TKE HHPI in flat terrain leads that in complex terrain by sometimes as much as 0.3 (Fig. B1b). Surface $\log_{10}\epsilon$ demonstrates the smallest flat terrain lead (Fig. B1c). These flat terrain leads, pronounced at the surface, are not guaranteed at higher heights. While L HHPI continues to reflect a flat terrain premium (Fig. B1a), both TKE HHPI (Fig. B1b) and $\log_{10}\epsilon$ HHPI (Fig. B1c) do not. Thus, while shorter towers may be more useful in flat terrain than in complex terrain, flat terrain towers may also benefit less from height increases.

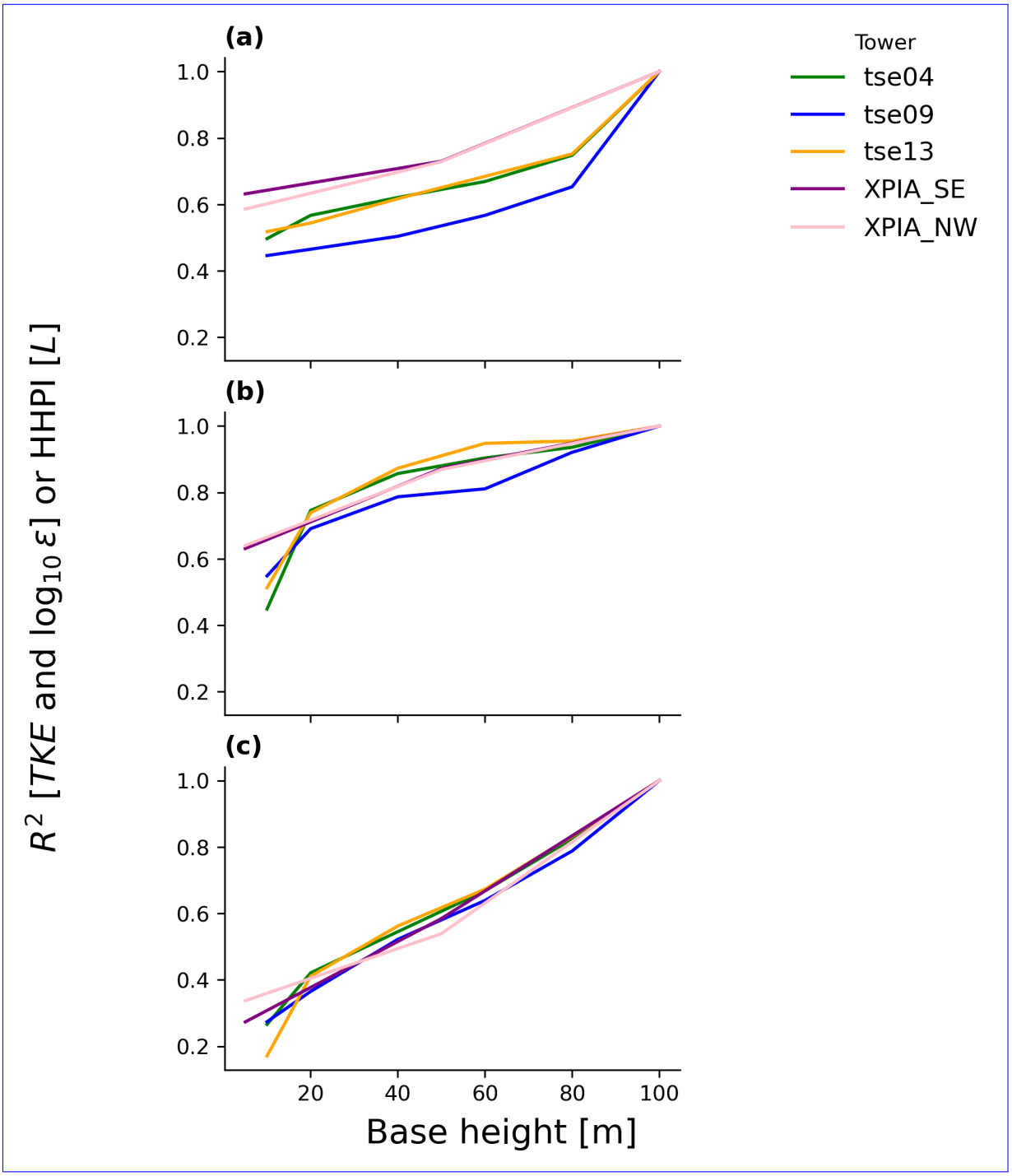

Figure B1. Flat terrain (XPIA) benchmark to the Perdigão HHPI analysis. (a) L; (b) TKE; (c) $\log_{10}\epsilon$.

Appendix C

Here we demonstrate a proof-of-concept implementation of the Louvain methodology applied to large-eddy simulation (LES) data. This Louvain implementation considers near-surface static stability from the LES of Robey and Lundquist (2024) (Table C1), based on Wise et al. (2021). These data represent a roughly 3 hr period early in the morning. Although simulation output is available at 1 second resolution, here we sample every 30 min, consistent with other analyses in this work. We also spatially coarsened the 100 m output to the effective model resolution of 500 m (Skamarock, 2004) and then subset to the identified Perdigão tower locations. Static stability was then calculated from these spatially- and temporally-coarsened data as:

$$\frac{\partial \theta}{\partial z} = \frac{\theta_2 - \theta_1}{z_2 - z_1} \tag{C1}$$

such that θ represents a potential temperature (K), z represents a model height above ground (m) and the two model levels taken are those closest to the surface (10 m and 2 m). The Louvain algorithm was then applied to these static stability calculations, resulting in seven partitions (Fig. C1). Overall, these tower groupings reflect broad terrain boundaries, with opportunities for mixing. Orange is predominately restricted to the upper valley. Dark blue exists mostly on ridges and the outer transects. The relatively small gray partition exists in the slope between the NE ridge and the valley. Light blue reflects most of the SW ridge, with occasional representation in the valley. The salmon, brown, and green transects are less geographically informed. Of course, because this analysis is based on 3 hours of LES during stably stratified conditions rather than the full measurement campaign period, the partitions are different from those presented in the main paper.

Table C1. Model parameters used in LES Louvain analysis, based on Robey and Lundquist (2024).

Model Parameter	**Value**0.5ex>0.5ex
Start time	2017-06-14 03:24:00
End time	2017-06-14 05:16:25
Effective horizontal resolution	500 m
Horizontal grid resolution	100 m
Vertical grid resolution	160 vertical levels
Vertical levels	2 m and 10 m
Land cover	CORINE Land Cover 2006 with mixed shrubland–grassland roughness length updated to 0.5 m
Terrain	1 arcsec terrain from the Shuttle Radar Topography Mission (SRTM)
Turbulence subgrid-scale model	non-linear backscatter and anistropy (NBA2)

This implementation is designed to serve several stakeholders and future research directions. Because this analysis builds on publicly available LES output from Robey and Lundquist (2024), it provides a reproducible benchmark for future Louvain or LES-based studies. The short duration and dense observations create opportunities to explore similarity metrics beyond the temporal correlation weight used here. We also introduce static stability as an alternate metric that depends only on temperature measurements, recognizing that many stakeholders, including wind farm developers, rely on sparse instrumentation. To further mimic these practical constraints, we adopt a 30-minute temporal resolution.

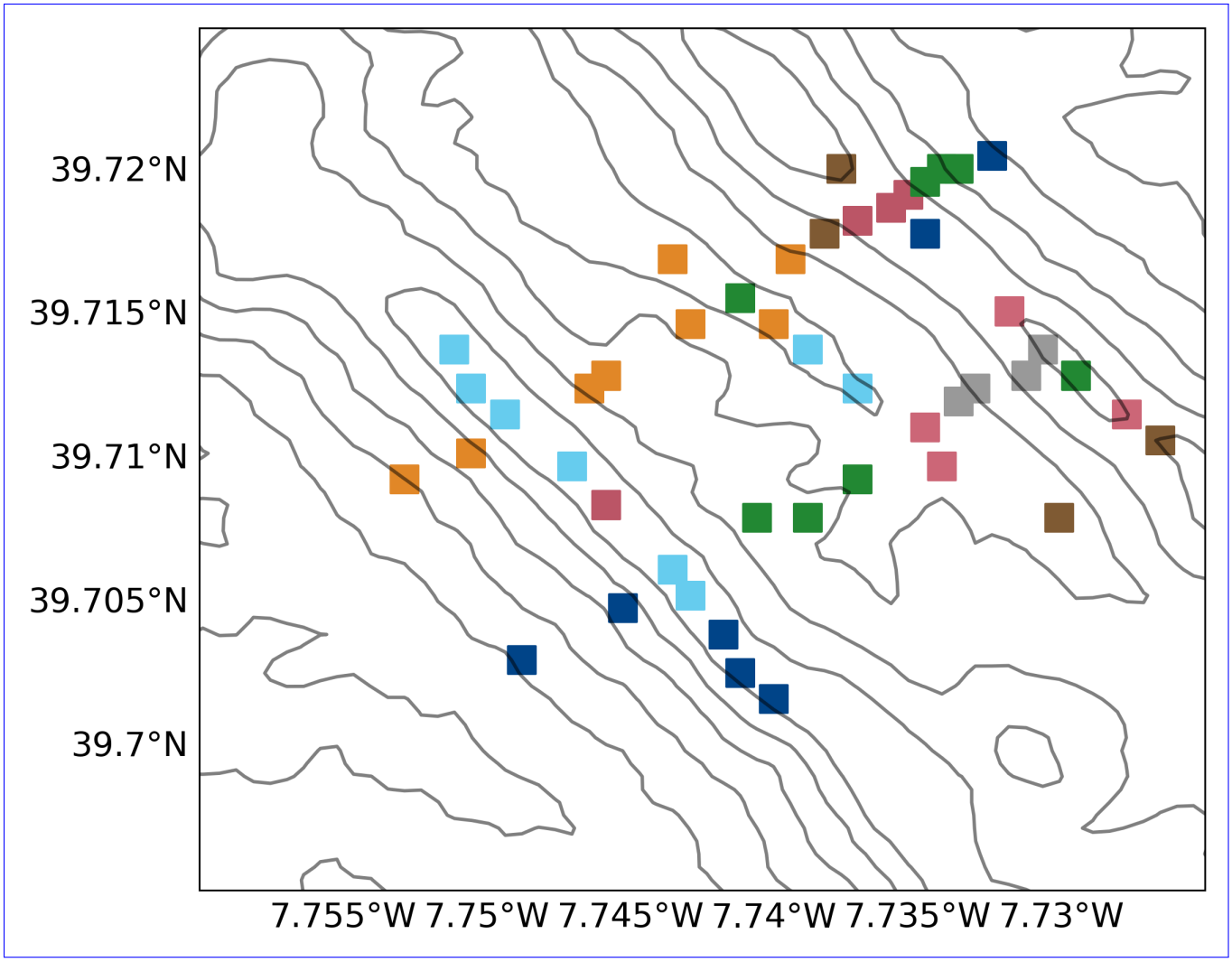

Figure C1. Static stability partitions determined by the Louvain community detection algorithm with LES output from Robey and Lundquist (2024) at the locations of the station towers. Model parameters are defined in Table C1.

This case study therefore provides both a benchmark and a flexible framework that can be extended to other datasets, parameterizations, and applications.

Author contributions. JKL: conceptualization, funding acquisition, investigation, project administration, supervision, writing - original draft, writing - review & editing. NJA: formal analysis, investigation, methodology, software, validation, visualization, writing - original draft and writing - review & editing.

Competing interests. At least one of the (co-)authors is a member of the editorial board of *Wind Energy Science*.

Acknowledgements. We thank Ivana Stiperski and Samuele Mosso for discussions on Reynolds decomposition intervals. This research has been supported by the U.S. National Science Foundation (grant no. AGS-1565498 and CAREER AGS-1554055). This work utilized the Alpine high performance computing resource at the University of Colorado Boulder. Alpine is jointly funded by the University of Colorado Boulder, the University of Colorado Anschutz, Colorado State University, and the National Science Foundation (award 2201538). This work was authored in part by the National ~~Renewable Energy Laboratory~~ Laboratory of the Rockies for the U.S. Department of Energy (DOE) under Contract No. DE-AC36-08GO28308. Funding provided by U.S. Department of Energy Office of ~~Energy Efficiency and Renewable Energy~~ Critical Minerals and Energy Innovation Wind Energy Technologies Office.. The views expressed in the article do not necessarily represent the views of the DOE or the U.S. Government. The U.S. Government retains and the publisher, by accepting the article for publication, acknowledges that the U.S. Government retains a nonexclusive, paid-up, irrevocable, worldwide license to publish or reproduce the published form of this work, or allow others to do so, for U.S. Government purposes.

References

Aitken, M. L., Banta, R. M., Pichugina, Y. L., and Lundquist, J. K.: Quantifying Wind Turbine Wake Characteristics from Scanning Remote Sensor Data, Journal of Atmospheric and Oceanic Technology, 31, 765 – 787, https://doi.org/10.1175/JTECH-D-13-00104.1, 2014.

Al Oqaily, D., Giani, P., and Crippa, P.: Evaluating WRF Multiscale Wind Simulations in Complex Terrain: Insights From the Perdigão Field Campaign, Journal of Geophysical Research: Atmospheres, 130, e2025JD044 055, https://doi.org/10.1029/2025JD044055, _eprint: https://agupubs.onlinelibrary.wiley.com/doi/pdf/10.1029/2025JD044055, 2025.

Anderson, K. S., Hansen, C. W., Holmgren, W. F., Jensen, A. R., Mikofski, M. A., and Driesse, A.: pvlib python: 2023 project update, Journal of Open Source Software, 8, 5994, https://doi.org/10.21105/joss.05994, 2023.

Angevine, W. M., Edwards, J. M., Lothon, M., LeMone, M. A., and Osborne, S. R.: Transition Periods in the Diurnally-Varying Atmospheric Boundary Layer Over Land, Boundary-Layer Meteorology, 177, 205–223, https://doi.org/10.1007/s10546-020-00515-y, 2020.

Aubinet, M., Vesala, T., and Papale, D., eds.: Eddy Covariance: A Practical Guide to Measurement and Data Analysis, Springer Netherlands, Dordrecht, https://doi.org/10.1007/978-94-007-2351-1, 2012.

Babić, K., Klaić, Z. B., and Večenaj, Z.: Determining a turbulence averaging time scale by Fourier analysis for the nocturnal boundary layer, 29, 2012.

Babić, K., Rotach, M. W., and Klaić, Z. B.: Evaluation of local similarity theory in the wintertime nocturnal boundary layer over heterogeneous surface, Agricultural and Forest Meteorology, 228-229, 164–179, https://doi.org/10.1016/j.agrformet.2016.07.002, 2016.

Bailey, B. H., McDonald, S. L., Bernadett, D. W., Markus, M. J., and Elsholz, K. V.: Wind resource assessment handbook: Fundamentals for conducting a successful monitoring program, Tech. Rep. NREL/SR-440-22223; ON: DE97000250, National Renewable Energy Lab. (NREL), Golden, CO (United States); AWS Scientific, Inc., Albany, NY (US), https://doi.org/10.2172/486127, 1997.

Baker, R. W. and Walker, S. N.: Wake measurements behind a large horizontal axis wind turbine generator, Solar Energy, 33, 5–12, https://doi.org/10.1016/0038-092X(84)90110-5, 1984.

Bardal, L. M., Sætran, L. R., and Wangsness, E.: Performance Test of a 3MW Wind Turbine – Effects of Shear and Turbulence, Energy Procedia, 80, 83–91, https://doi.org/10.1016/j.egypro.2015.11.410, 2015.

Barthelmie, R. J. and Pryor, S. C.: Automated wind turbine wake characterization in complex terrain, Atmospheric Measurement Techniques, 12, 3463–3484, https://doi.org/10.5194/amt-12-3463-2019, publisher: Copernicus GmbH, 2019.

Barthelmie, R. J., Hansen, K. S., and Pryor, S. C.: Meteorological Controls on Wind Turbine Wakes, Proceedings of the IEEE, 101, 1010–1019, https://doi.org/10.1109/JPROC.2012.2204029, 2013.

Bell, T. M., Klein, P., Wildmann, N., and Menke, R.: Analysis of flow in complex terrain using multi-Doppler lidar retrievals, Atmospheric Measurement Techniques, 13, 1357–1371, https://doi.org/10.5194/amt-13-1357-2020, publisher: Copernicus GmbH, 2020.

Blondel, V. D., Guillaume, J.-L., Lambiotte, R., and Lefebvre, E.: Fast unfolding of communities in large networks, Journal of Statistical Mechanics: Theory and Experiment, 2008, P10 008, https://doi.org/10.1088/1742-5468/2008/10/P10008, 2008.

Bodini, N., Zardi, D., and Lundquist, J. K.: Three-dimensional structure of wind turbine wakes as measured by scanning lidar, Atmospheric Measurement Techniques, 10, 2881–2896, https://doi.org/10.5194/amt-10-2881-2017, publisher: Copernicus GmbH, 2017.

Bodini, N., Lundquist, J. K., and Newsom, R. K.: Estimation of turbulence dissipation rate and its variability from sonic anemometer and wind Doppler lidar during the XPIA field campaign, Atmospheric Measurement Techniques, 11, 4291–4308, https://doi.org/10.5194/amt-11-4291-2018, publisher: Copernicus GmbH, 2018.

Bodini, N., Lundquist, J. K., and Kirincich, A.: U.S. East Coast Lidar Measurements Show Offshore Wind Turbines Will Encounter Very Low Atmospheric Turbulence, Geophysical Research Letters, 46, 5582–5591, https://doi.org/10.1029/2019GL082636, _eprint: https://onlinelibrary.wiley.com/doi/pdf/10.1029/2019GL082636, 2019.

Bodini, N., Lundquist, J. K., and Optis, M.: Can machine learning improve the model representation of turbulent kinetic energy dissipation rate in the boundary layer for complex terrain?, Geoscientific Model Development, 13, 4271–4285, https://doi.org/10.5194/gmd-13-4271-2020, publisher: Copernicus GmbH, 2020.

Bossard, M., Feranec, J., and Ot'ahel', J.: Corine Land Cover—Technical Guide, 2000.

Brock, F. V., Crawford, K. C., Elliott, R. L., Cuperus, G. W., Stadler, S. J., Johnson, H. L., and Eilts, M. D.: The Oklahoma Mesonet: A Technical Overview, Journal of Atmospheric and Oceanic Technology, 12, 5–19, https://doi.org/10.1175/1520-0426(1995)012<0005:TOMATO>2.0.CO;2, 1995.

Brotzge, J. A., Wang, J., Thorncroft, C. D., Joseph, E., Bain, N., Bassill, N., Farruggio, N., Freedman, J. M., Hemker, K., Johnston, D., Kane, E., McKim, S., Miller, S. D., Minder, J. R., Naple, P., Perez, S., Schwab, J. J., Schwab, M. J., and Sicker, J.: A Technical Overview of the New York State Mesonet Standard Network, https://doi.org/10.1175/JTECH-D-19-0220.1, section: Journal of Atmospheric and Oceanic Technology, 2020.

Brugger, P., Fuertes, F. C., Vahidzadeh, M., Markfort, C. D., and Porté-Agel, F.: Characterization of Wind Turbine Wakes with Nacelle-Mounted Doppler LiDARs and Model Validation in the Presence of Wind Veer, Remote Sensing, 11, 2247, https://doi.org/10.3390/rs11192247, number: 19 Publisher: Multidisciplinary Digital Publishing Institute, 2019.

Burns, S. P., Horst, T. W., Jacobsen, L., Blanken, P. D., and Monson, R. K.: Using sonic anemometer temperature to measure sensible heat flux in strong winds, Atmospheric Measurement Techniques, 5, 2095–2111, https://doi.org/10.5194/amt-5-2095-2012, publisher: Copernicus GmbH, 2012.

Cantero, E., Sanz, J., Borbón, F., Paredes, D., and García, A.: On the measurement of stability parameter over complex mountainous terrain, Wind Energy Science, 7, 221–235, https://doi.org/10.5194/wes-7-221-2022, publisher: Copernicus GmbH, 2022.

Churchfield, M. J. and Sirnivas, S.: On the Effects of Wind Turbine Wake Skew Caused by Wind Veer, in: 2018 Wind Energy Symposium, AIAA SciTech Forum, American Institute of Aeronautics and Astronautics, https://doi.org/10.2514/6.2018-0755, 2018.

Clifton, A., Barber, S., Stökl, A., Frank, H., and Karlsson, T.: Research challenges and needs for the deployment of wind energy in hilly and mountainous regions, Wind Energy Science, 7, 2231–2254, https://doi.org/10.5194/wes-7-2231-2022, 2022.

Coimbra, I. L., Mann, J., Palma, J. M. L. M., and Batista, V. T. P.: Exploring dual-lidar mean and turbulence measurements over Perdigão's complex terrain, Atmospheric Measurement Techniques, 18, 287–303, https://doi.org/10.5194/amt-18-287-2025, publisher: Copernicus GmbH, 2025.

Connolly, A., van Veen, L., Neher, J., Geurts, B. J., Mirocha, J., and Chow, F. K.: Efficacy of the Cell Perturbation Method in Large-Eddy Simulations of Boundary Layer Flow over Complex Terrain, Atmosphere, 12, 55, https://doi.org/10.3390/atmos12010055, publisher: Multidisciplinary Digital Publishing Institute, 2021.

Dar, A. S., Berg, J., Troldborg, N., and Patton, E. G.: On the self-similarity of wind turbine wakes in a complex terrain using large eddy simulation, Wind Energy Science, 4, 633–644, https://doi.org/10.5194/wes-4-633-2019, publisher: Copernicus GmbH, 2019.

Desjardins, R. L., MacPherson, J. I., Schuepp, P. H., and Karanja, F.: An evaluation of aircraft flux measurements of CO2, water vapor and sensible heat, Boundary-Layer Meteorology, 47, 55–69, https://doi.org/10.1007/BF00122322, 1989.

Dimitrov, N., Kelly, M. C., Vignaroli, A., and Berg, J.: From wind to loads: wind turbine site-specific load estimation with surrogate models trained on high-fidelity load databases, Wind Energy Science, 3, 767–790, https://doi.org/10.5194/wes-3-767-2018, publisher: Copernicus GmbH, 2018.

DTU Wind and Energy Systems: The Perdigao 2017 Field Experiment, https://www.youtube.com/watch?v=rd3MUG715Bs, 2017.

Eberle, A., Roberts, J. O., Key, A., Bhaskar, P., and Dykes, K. L.: NREL's Balance-of-System Cost Model for Land-Based Wind, Tech. Rep. NREL/TP-6A20-72201, 1569457, https://doi.org/10.2172/1569457, 2019.

Elliott, D. L.: EFFECTS OF WIND SHEAR AND TURBULENCE ON WIND TURBINE POWER CURVES, 1990.

Englberger, A. and Dörnbrack, A.: Impact of the Diurnal Cycle of the Atmospheric Boundary Layer on Wind-Turbine Wakes: A Numerical Modelling Study, Boundary-Layer Meteorology, 166, 423–448, https://doi.org/10.1007/s10546-017-0309-3, 2018.

EOL: Perdigao photos | Earth Observing Laboratory, https://www.eol.ucar.edu/content/perdigao-photos.

EOL, U.: NCAR/EOL Quality Controlled High-rate ISFS surface flux data, geographic coordinate, tilt corrected. Version 1.1, https://doi.org/10.26023/8X1N-TCT4-P50X, artwork Size: 172 data files, 1 ancillary/documentation file, 314 GiB Pages: 172 data files, 1 ancillary/documentation file, 314 GiB, 2019.

Fernando, H. J. S., Mann, J., Palma, J. M. L. M., Lundquist, J. K., Barthelmie, R. J., Belo-Pereira, M., Brown, W. O. J., Chow, F. K., Gerz, T., Hocut, C. M., Klein, P. M., Leo, L. S., Matos, J. C., Oncley, S. P., Pryor, S. C., Bariteau, L., Bell, T. M., Bodini, N., Carney, M. B., Courtney, M. S., Creegan, E. D., Dimitrova, R., Gomes, S., Hagen, M., Hyde, J. O., Kigle, S., Krishnamurthy, R., Lopes, J. C., Mazzaro, L., Neher, J. M. T., Menke, R., Murphy, P., Oswald, L., Otarola-Bustos, S., Pattantyus, A. K., Rodrigues, C. V., Schady, A., Sirin, N., Spuler, S., Svensson, E., Tomaszewski, J., Turner, D. D., Veen, L. v., Vasiljević, N., Vassallo, D., Voss, S., Wildmann, N., and Wang, Y.: The Perdigão: Peering into Microscale Details of Mountain Winds, Bulletin of the American Meteorological Society, 100, 799–819, https://doi.org/10.1175/BAMS-D-17-0227.1, publisher: American Meteorological Society Section: Bulletin of the American Meteorological Society, 2019.

Gao, L., Li, B., and Hong, J.: Effect of wind veer on wind turbine power generation, Physics of Fluids, 33, 015 101, https://doi.org/10.1063/5.0033826, 2021.

Garratt, J. R.: Review: the atmospheric boundary layer, Earth-Science Reviews, 37, 89–134, https://doi.org/10.1016/0012-8252(94)90026-4, 1994.

Giani, P. and Crippa, P.: On the Sensitivity of Large-Eddy Simulations of the Atmospheric Boundary Layer Coupled with Realistic Large-Scale Dynamics, https://doi.org/10.1175/MWR-D-23-0101.1, section: Monthly Weather Review, 2024.

Goit, J. P., Taguchi, M., Tatsuno, J., and Kameda, T.: Effect of averaging time windows on wind resource assessment of small wind turbines, Wind Energy, 25, 1222–1237, https://doi.org/10.1002/we.2723, _eprint: https://onlinelibrary.wiley.com/doi/pdf/10.1002/we.2723, 2022.

Gryning, S.-E., Batchvarova, E., Brümmer, B., Jørgensen, H., and Larsen, S.: On the extension of the wind profile over homogeneous terrain beyond the surface boundary layer, Boundary-Layer Meteorology, 124, 251–268, https://doi.org/10.1007/s10546-007-9166-9, 2007.

Hagberg, A. A., Schult, D. A., and Swart, P. J.: Exploring Network Structure, Dynamics, and Function using NetworkX, in: Proceedings of the 7th Python in Science Conference, edited by Varoquaux, G., Vaught, T., and Millman, J., pp. 11 – 15, Pasadena, CA USA, 2008.

Han, X., Liu, D., Xu, C., and Shen, W. Z.: Atmospheric stability and topography effects on wind turbine performance and wake properties in complex terrain, Renewable Energy, 126, 640–651, https://doi.org/10.1016/j.renene.2018.03.048, 2018.

Howell, J. F. and Mahrt, L.: An Adaptive Multiresolution Data Filter: Applications to Turbulence and Climatic Time Series, Journal of the Atmospheric Sciences, 51, 2165–2178, https://doi.org/10.1175/1520-0469(1994)051<2165:AAMDFA>2.0.CO;2, publisher: American Meteorological Society Section: Journal of the Atmospheric Sciences, 1994.

Howell, J. F. and Mahrt, L.: Multiresolution Flux Decomposition, Boundary-Layer Meteorology, 83, 117–137, https://doi.org/10.1023/A:1000210427798, 1997.

IEC: IEC 61400-12-1:2022, https://webstore.iec.ch/en/publication/68499.

Ineichen, P. and Perez, R.: A new airmass independent formulation for the Linke turbidity coefficient, Solar Energy, 73, 151–157, https://doi.org/10.1016/S0038-092X(02)00045-2, 2002.

Iungo, G. V. and Porté-Agel, F.: Volumetric Lidar Scanning of Wind Turbine Wakes under Convective and Neutral Atmospheric Stability Regimes, Journal of Atmospheric and Oceanic Technology, 31, 2035–2048, https://doi.org/10.1175/JTECH-D-13-00252.1, publisher: American Meteorological Society Section: Journal of Atmospheric and Oceanic Technology, 2014.

Kang, S.-L. and Won, H.: Spectral structure of 5 year time series of horizontal wind speed at the Boulder Atmospheric Observatory, Journal of Geophysical Research: Atmospheres, 121, 11,946–11,967, https://doi.org/10.1002/2016JD025289, _eprint: https://onlinelibrary.wiley.com/doi/pdf/10.1002/2016JD025289, 2016.

Karp, R. M.: Reducibility Among Combinatorial Problems, in: Complexity of Computer Computations, edited by Miller, R. E. and Thatcher, J. W., pp. 85–103, Plenum Press, New York, 1972.

Keck, R.-E., de Maré, M., Churchfield, M. J., Lee, S., Larsen, G., and Aagaard Madsen, H.: On atmospheric stability in the dynamic wake meandering model, Wind Energy, 17, 1689–1710, https://doi.org/10.1002/we.1662, _eprint: https://onlinelibrary.wiley.com/doi/pdf/10.1002/we.1662, 2014.

Lange, J., Mann, J., Berg, J., Parvu, D., Kilpatrick, R., Costache, A., Chowdhury, J., Siddiqui, K., and Hangan, H.: For wind turbines in complex terrain, the devil is in the detail, Environmental Research Letters, 12, 094 020, https://doi.org/10.1088/1748-9326/aa81db, publisher: IOP Publishing, 2017.

Larsen, G. C., Ott, S., Larsen, T. J., Hansen, K. S., and Chougule, A.: Improved modelling of fatigue loads in wind farms under non-neutral ABL stability conditions, Journal of Physics: Conference Series, 1037, 072 013, https://doi.org/10.1088/1742-6596/1037/7/072013, publisher: IOP Publishing, 2018.

Larsén, X. G., Vincent, C., and Larsen, S.: Spectral structure of mesoscale winds over the water, Quarterly Journal of the Royal Meteorological Society, 139, 685–700, https://doi.org/10.1002/qj.2003, _eprint: https://onlinelibrary.wiley.com/doi/pdf/10.1002/qj.2003, 2013.

Lee, J. C. Y., Stuart, P., Clifton, A., Fields, M. J., Perr-Sauer, J., Williams, L., Cameron, L., Geer, T., and Housley, P.: The Power Curve Working Group's assessment of wind turbine power performance prediction methods, Wind Energy Science, 5, 199–223, https://doi.org/10.5194/wes-5-199-2020, publisher: Copernicus GmbH, 2020.

Letson, F., Barthelmie, R. J., Hu, W., and Pryor, S. C.: Characterizing wind gusts in complex terrain, Atmospheric Chemistry and Physics, 19, 3797–3819, https://doi.org/10.5194/acp-19-3797-2019, publisher: Copernicus GmbH, 2019.

Lundquist, J. K.: Wind Shear and Wind Veer Effects on Wind Turbines, in: Handbook of Wind Energy Aerodynamics, edited by Stoevesandt, B., Schepers, G., Fuglsang, P., and Sun, Y., pp. 859–880, Springer International Publishing, Cham, https://doi.org/10.1007/978-3-030-31307-4_44, 2022.

Lundquist, J. K., Wilczak, J. M., Ashton, R., Bianco, L., Brewer, W. A., Choukulkar, A., Clifton, A., Debnath, M., Delgado, R., Friedrich, K., Gunter, S., Hamidi, A., Iungo, G. V., Kaushik, A., Kosović, B., Langan, P., Lass, A., Lavin, E., Lee, J. C.-Y., McCaffrey, K. L., Newsom, R. K., Noone, D. C., Oncley, S. P., Quelet, P. T., Sandberg, S. P., Schroeder, J. L., Shaw, W. J., Sparling, L., Martin, C. S., Pe, A. S., Strobach, E., Tay, K., Vanderwende, B. J., Weickmann, A., Wolfe, D., and Worsnop, R.: Assessing State-of-the-Art Capabilities for Probing the Atmospheric Boundary Layer: The XPIA Field Campaign, https://doi.org/10.1175/BAMS-D-15-00151.1, section: Bulletin of the American Meteorological Society, 2017.

Magnusson, M. and Smedman, A.-S.: Influence of Atmospheric Stability on Wind Turbine Wakes, Wind Engineering, 18, 139–152, https://www.jstor.org/stable/43749538, publisher: Sage Publications, Ltd., 1994.

Mahrt, L.: Stratified Atmospheric Boundary Layers, Boundary-Layer Meteorology, 90, 375–396, https://doi.org/10.1023/A:1001765727956, 1999.

McCaffrey, K., Quelet, P. T., Choukulkar, A., Wilczak, J. M., Wolfe, D. E., Oncley, S. P., Brewer, W. A., Debnath, M., Ashton, R., Iungo, G. V., and Lundquist, J. K.: Identification of tower-wake distortions using sonic anemometer and lidar measurements, Atmospheric Measurement Techniques, 10, 393–407, https://doi.org/10.5194/amt-10-393-2017, publisher: Copernicus GmbH, 2017.

Menke, R., Vasiljević, N., Hansen, K. S., Hahmann, A. N., and Mann, J.: Does the wind turbine wake follow the topography? A multi-lidar study in complex terrain, Wind Energy Science, 3, 681–691, https://doi.org/10.5194/wes-3-681-2018, publisher: Copernicus GmbH, 2018.

Menke, R., Vasiljević, N., Mann, J., and Lundquist, J. K.: Characterization of flow recirculation zones at the Perdigão site using multi-lidar measurements, Atmospheric Chemistry and Physics, 19, 2713–2723, https://doi.org/10.5194/acp-19-2713-2019, publisher: Copernicus GmbH, 2019.

Mitchell, S., O'Sullivan, M., and Dunning, I.: PuLP: A linear programming toolkit for Python, Tech. rep., Department of Engineering Science, The University of Auckland, 2011.

Monin, A. S. and Obukhov, A. M.: Basic laws of turbulent mixing in the surface layer of the atmosphere, 1954.

Mosso, S., Calaf, M., and Stiperski, I.: Flux-gradient relations and their dependence on turbulence anisotropy, Quarterly Journal of the Royal Meteorological Society, 150, 3346–3367, https://doi.org/10.1002/qj.4762, _eprint: https://onlinelibrary.wiley.com/doi/pdf/10.1002/qj.4762, 2024.

Mosso, S., Lapo, K., and Stiperski, I.: Revealing the drivers of turbulence anisotropy over flat and complex terrain: an interpretable machine learning approach, https://doi.org/10.48550/arXiv.2503.15276, arXiv:2503.15276 [physics], 2025.

Muñoz-Esparza, D., Kosović, B., van Beeck, J., and Mirocha, J.: A stochastic perturbation method to generate inflow turbulence in large-eddy simulation models: Application to neutrally stratified atmospheric boundary layers, Physics of Fluids, 27, 035 102, https://doi.org/10.1063/1.4913572, 2015.

Muñoz-Esparza, D., Sharman, R. D., and Lundquist, J. K.: Turbulence Dissipation Rate in the Atmospheric Boundary Layer: Observations and WRF Mesoscale Modeling during the XPIA Field Campaign, Monthly Weather Review, 146, 351–371, https://doi.org/10.1175/MWR-D-17-0186.1, publisher: American Meteorological Society Section: Monthly Weather Review, 2018.

Olson, J. B., Kenyon, J. S., Djalalova, I., Bianco, L., Turner, D. D., Pichugina, Y., Choukulkar, A., Toy, M. D., Brown, J. M., Angevine, W. M., Akish, E., Bao, J.-W., Jimenez, P., Kosovic, B., Lundquist, K. A., Draxl, C., Lundquist, J. K., McCaa, J., McCaffrey, K., Lantz, K., Long, C., Wilczak, J., Banta, R., Marquis, M., Redfern, S., Berg, L. K., Shaw, W., and Cline, J.: Improving Wind Energy Forecasting through Numerical Weather Prediction Model Development, Bulletin of the American Meteorological Society, 100, 2201–2220, https://doi.org/10.1175/BAMS-D-18-0040.1, publisher: American Meteorological Society Section: Bulletin of the American Meteorological Society, 2019.

Oncley, S. P., Friehe, C. A., Larue, J. C., Businger, J. A., Itsweire, E. C., and Chang, S. S.: Surface-Layer Fluxes, Profiles, and Turbulence Measurements over Uniform Terrain under Near-Neutral Conditions, Journal of the Atmospheric Sciences, 53, 1029–1044, https://doi.org/10.1175/1520-0469(1996)053<1029:SLFPAT>2.0.CO;2, publisher: American Meteorological Society Section: Journal of the Atmospheric Sciences, 1996.

Optis, M. and Perr-Sauer, J.: The importance of atmospheric turbulence and stability in machine-learning models of wind farm power production, Renewable and Sustainable Energy Reviews, 112, 27–41, https://doi.org/10.1016/j.rser.2019.05.031, 2019.

Palma, J. M. L. M., Silva, C. A. M., Gomes, V. C., Silva Lopes, A., Simões, T., Costa, P., and Batista, V. T. P.: The digital terrain model in the computational modelling of the flow over the Perdigão site: the appropriate grid size, Wind Energy Science, 5, 1469–1485, https://doi.org/10.5194/wes-5-1469-2020, publisher: Copernicus GmbH, 2020.

Parker, M. J. and Raman, S.: A case study of the nocturnal boundary layer over a complex terrain, Boundary-Layer Meteorology, 66, 303–324, https://doi.org/10.1007/BF00705480, 1993.

Pineda, N., Jorba, O., Jorge, J., and Baldasano, J.: Using NOAA AVHRR and SPOT VGT data to estimate surface parameters: application to a mesoscale meteorological model, International Journal of Remote Sensing - INT J REMOTE SENS, 25, 129–143, https://doi.org/10.1080/0143116031000115201, 2004.

Piper, M. and Lundquist, J. K.: Surface Layer Turbulence Measurements during a Frontal Passage, Journal of the Atmospheric Sciences, 61, 1768–1780, https://doi.org/10.1175/1520-0469(2004)061<1768:SLTMDA>2.0.CO;2, publisher: American Meteorological Society Section: Journal of the Atmospheric Sciences, 2004.

Putri, R. M., Obhrai, C., and Knight, J. M.: Offshore Wind Turbine Loads and Motions in Unstable Atmospheric Conditions, Journal of Physics: Conference Series, 1356, 012 016, https://doi.org/10.1088/1742-6596/1356/1/012016, publisher: IOP Publishing, 2019.

Pérez, C., Rivero, M., Escalante, M., Ramirez, V., and Guilbert, D.: Influence of Atmospheric Stability on Wind Turbine Energy Production: A Case Study of the Coastal Region of Yucatan, Energies, 16, 4134, https://doi.org/10.3390/en16104134, 2023.

Pérez Albornoz, C., Escalante Soberanis, M. A., Ramírez Rivera, V., and Rivero, M.: Review of atmospheric stability estimations for wind power applications, Renewable and Sustainable Energy Reviews, 163, 112 505, https://doi.org/10.1016/j.rser.2022.112505, 2022.

Quimbayo-Duarte, J., Wagner, J., Wildmann, N., Gerz, T., and Schmidli, J.: Evaluation of a forest parameterization to improve boundary layer flow simulations over complex terrain. A case study using WRF-LES V4.0.1, Geoscientific Model Development, 15, 5195–5209, https://doi.org/10.5194/gmd-15-5195-2022, publisher: Copernicus GmbH, 2022.

Radünz, W. C., Sakagami, Y., Haas, R., Petry, A. P., Passos, J. C., Miqueletti, M., and Dias, E.: Influence of atmospheric stability on wind farm performance in complex terrain, Applied Energy, 282, 116 149, https://doi.org/10.1016/j.apenergy.2020.116149, 2021.

Reynolds, O.: IV. On the dynamical theory of incompressible viscous fluids and the determination of the criterion, Philosophical Transactions of the Royal Society of London. (A.), 186, 123–164, https://doi.org/10.1098/rsta.1895.0004, publisher: Royal Society, 1895.

Robertson, A. N., Shaler, K., Sethuraman, L., and Jonkman, J.: Sensitivity analysis of the effect of wind characteristics and turbine properties on wind turbine loads, Wind Energy Science, 4, 479–513, https://doi.org/10.5194/wes-4-479-2019, publisher: Copernicus GmbH, 2019.

Robey, R. and Lundquist, J. K.: Behavior and mechanisms of Doppler wind lidar error in varying stability regimes, Atmospheric Measurement Techniques, 15, 4585–4622, https://doi.org/10.5194/amt-15-4585-2022, publisher: Copernicus GmbH, 2022.

Robey, R. and Lundquist, J. K.: Influences of lidar scanning parameters on wind turbine wake retrievals in complex terrain, Wind Energy Science, 9, 1905–1922, https://doi.org/10.5194/wes-9-1905-2024, publisher: Copernicus GmbH, 2024.

Sanchez Gomez, M. and Lundquist, J. K.: The effect of wind direction shear on turbine performance in a wind farm in central Iowa, Wind Energy Science, 5, 125–139, https://doi.org/10.5194/wes-5-125-2020, publisher: Copernicus GmbH, 2020.

Santos, J. A., Belo-Pereira, M., Fraga, H., and Pinto, J. G.: Understanding climate change projections for precipitation over western Europe with a weather typing approach, Journal of Geophysical Research: Atmospheres, 121, 1170–1189, https://doi.org/10.1002/2015JD024399, _eprint: https://agupubs.onlinelibrary.wiley.com/doi/pdf/10.1002/2015JD024399, 2016.

Sathe, A., Mann, J., Barlas, T., Bierbooms, W., and van Bussel, G.: Influence of atmospheric stability on wind turbine loads, Wind Energy, 16, 1013–1032, https://doi.org/10.1002/we.1528, _eprint: https://onlinelibrary.wiley.com/doi/pdf/10.1002/we.1528, 2013.

Serafin, S., Adler, B., Cuxart, J., De Wekker, S. F. J., Gohm, A., Grisogono, B., Kalthoff, N., Kirshbaum, D. J., Rotach, M. W., Schmidli, J., Stiperski, I., Večenaj, Z., and Zardi, D.: Exchange Processes in the Atmospheric Boundary Layer Over Mountainous Terrain, Atmosphere, 9, 102, https://doi.org/10.3390/atmos9030102, number: 3 Publisher: Multidisciplinary Digital Publishing Institute, 2018.

Sfyri, E., Rotach, M. W., Stiperski, I., Bosveld, F. C., Lehner, M., and Obleitner, F.: Scalar-Flux Similarity in the Layer Near the Surface Over Mountainous Terrain, Boundary-Layer Meteorology, 169, 11–46, https://doi.org/10.1007/s10546-018-0365-3, 2018.

Shaw, W. J., Berg, L. K., Cline, J., Draxl, C., Djalalova, I., Grimit, E. P., Lundquist, J. K., Marquis, M., McCaa, J., Olson, J. B., Sivaraman, C., Sharp, J., and Wilczak, J. M.: The Second Wind Forecast Improvement Project (WFIP2): General Overview, Bulletin of the American Meteorological Society, 100, 1687–1699, https://doi.org/10.1175/BAMS-D-18-0036.1, publisher: American Meteorological Society Section: Bulletin of the American Meteorological Society, 2019.

Skamarock, W. C.: Evaluating Mesoscale NWP Models Using Kinetic Energy Spectra, Monthly Weather Review, 132, 3019–3032, https://doi.org/10.1175/MWR2830.1, publisher: American Meteorological Society Section: Monthly Weather Review, 2004.

Stiperski, I. and Rotach, M. W.: On the Measurement of Turbulence Over Complex Mountainous Terrain, Boundary-Layer Meteorology, 159, 97–121, https://doi.org/10.1007/s10546-015-0103-z, 2016.

Stull, R. B., ed.: An Introduction to Boundary Layer Meteorology, Springer Netherlands, Dordrecht, https://doi.org/10.1007/978-94-009-3027-8, 1988.

Tang, Q., Zhang, R., Chen, L., Deng, W., Xu, M., Xu, G., and Li, L.: Influence of the atmospheric boundary layer stability on aerial spraying studied by computational fluid dynamics, Biosystems Engineering, 215, 170–187, https://doi.org/10.1016/j.biosystemseng.2022.01.007, 2022.

Van der Hoven, I.: POWER SPECTRUM OF HORIZONTAL WIND SPEED IN THE FREQUENCY RANGE FROM 0.0007 TO 900 CYCLES PER HOUR, https://journals.ametsoc.org/view/journals/atsc/14/2/1520-0469_1957_014_0160_psohws_2_0_co_2.xml, section: Journal of the Atmospheric Sciences, 1957.

Vanderwende, B. J. and Lundquist, J. K.: The modification of wind turbine performance by statistically distinct atmospheric regimes, Environmental Research Letters, 7, 034 035, https://doi.org/10.1088/1748-9326/7/3/034035, publisher: IOP Publishing, 2012.

Vasiljević, N., L. M. Palma, J. M., Angelou, N., Carlos Matos, J., Menke, R., Lea, G., Mann, J., Courtney, M., Frölen Ribeiro, L., and M. G. C. Gomes, V. M.: Perdigão 2015: methodology for atmospheric multi-Doppler lidar experiments, Atmospheric Measurement Techniques, 10, 3463–3483, https://doi.org/10.5194/amt-10-3463-2017, 2017.

Vassallo, D., Krishnamurthy, R., and Fernando, H. J. S.: Decreasing wind speed extrapolation error via domain-specific feature extraction and selection, Wind Energy Science, 5, 959–975, https://doi.org/10.5194/wes-5-959-2020, publisher: Copernicus GmbH, 2020.

Venkatraman, K., Hågbo, T.-O., Buckingham, S., and Teigen Giljarhus, K. E.: Effect of different source terms and inflow direction in atmospheric boundary modeling over the complex terrain site of Perdigão, Wind Energy Science, 8, 85–108, https://doi.org/10.5194/wes-8-85-2023, publisher: Copernicus GmbH, 2023.

Vollmer, L., Steinfeld, G., Heinemann, D., and Kühn, M.: Estimating the wake deflection downstream of a wind turbine in different atmospheric stabilities: an LES study, Wind Energy Science, 1, 129–141, https://doi.org/https://doi.org/10.5194/wes-1-129-2016, 2016.

Wagner, J., Gerz, T., Wildmann, N., and Gramitzky, K.: Long-term simulation of the boundary layer flow over the double-ridge site during the Perdigão 2017 field campaign, Atmospheric Chemistry and Physics, 19, 1129–1146, https://doi.org/10.5194/acp-19-1129-2019, publisher: Copernicus GmbH, 2019.

Wharton, S. and Lundquist, J. K.: Atmospheric stability affects wind turbine power collection, Environmental Research Letters, 7, 014 005, https://doi.org/10.1088/1748-9326/7/1/014005, publisher: IOP Publishing, 2012.

Wilczak, J. M., Oncley, S. P., and Stage, S. A.: Sonic Anemometer Tilt Correction Algorithms, Boundary-Layer Meteorology, 99, 127–150, https://doi.org/10.1023/A:1018966204465, 2001.

Wildmann, N., Bodini, N., Lundquist, J. K., Bariteau, L., and Wagner, J.: Estimation of turbulence dissipation rate from Doppler wind lidars and in situ instrumentation for the Perdigão 2017 campaign, Atmospheric Measurement Techniques, 12, 6401–6423, https://doi.org/10.5194/amt-12-6401-2019, publisher: Copernicus GmbH, 2019.

Wise, A. S., Neher, J. M. T., Arthur, R. S., Mirocha, J. D., Lundquist, J. K., and Chow, F. K.: Meso- to micro-scale modeling of atmospheric stability effects on wind turbine wake behavior in complex terrain, Wind Energy Science Discussions, pp. 1–36, https://doi.org/10.5194/wes-2021-36, publisher: Copernicus GmbH, 2021.